



AFRL-AFOSR-VA-TR-2015-0314

---

**Computational -Experimental Processing of Boride/Carbide Composites by Reactive Infusion of Hf Alloy Melts into B4C**

**Arturo Bronson  
UNIVERSITY OF TEXAS AT EL PASO**

---

**09/16/2015  
Final Report**

DISTRIBUTION A: Distribution approved for public release.

Air Force Research Laboratory  
AF Office Of Scientific Research (AFOSR)/ RTB1  
Arlington, Virginia 22203  
Air Force Materiel Command

<b>REPORT DOCUMENTATION PAGE</b>					Form Approved OMB No. 0704-0188	
<p>The public reporting burden for this collection of information is estimated to average 1 hour per response, including the time for reviewing instructions, searching existing data sources, gathering and maintaining the data needed, and completing and reviewing the collection of information. Send comments regarding this burden estimate or any other aspect of this collection of information, including suggestions for reducing the burden, to Department of Defense, Executive Services, Directorate (0704-0188). Respondents should be aware that notwithstanding any other provision of law, no person shall be subject to any penalty for failing to comply with a collection of information if it does not display a currently valid OMB control number.</p> <p>PLEASE DO NOT RETURN YOUR FORM TO THE ABOVE ORGANIZATION.</p>						
<b>1. REPORT DATE (DD-MM-YYYY)</b> 08-10-2015		<b>2. REPORT TYPE</b> Final Performance		<b>3. DATES COVERED (From - To)</b> 01-05-2012 to 30-04-2015		
<b>4. TITLE AND SUBTITLE</b> Computational -Experimental Processing of Boride/Carbide Composites by Reactive Infusion of Hf Alloy Melts into B4C				<b>5a. CONTRACT NUMBER</b>		
				<b>5b. GRANT NUMBER</b> FA9550-12-1-0242		
				<b>5c. PROGRAM ELEMENT NUMBER</b> 61102F		
<b>6. AUTHOR(S)</b> Arturo Bronson				<b>5d. PROJECT NUMBER</b>		
				<b>5e. TASK NUMBER</b>		
				<b>5f. WORK UNIT NUMBER</b>		
<b>7. PERFORMING ORGANIZATION NAME(S) AND ADDRESS(ES)</b> UNIVERSITY OF TEXAS AT EL PASO 500 UNIV ST ADMIN BLDG 209 EL PASO, TX 79968-0001 US				<b>8. PERFORMING ORGANIZATION REPORT NUMBER</b>		
<b>9. SPONSORING/MONITORING AGENCY NAME(S) AND ADDRESS(ES)</b> AF Office of Scientific Research 875 N. Randolph St. Room 3112 Arlington, VA 22203				<b>10. SPONSOR/MONITOR'S ACRONYM(S)</b> AFRL/AFOSR RTB1		
				<b>11. SPONSOR/MONITOR'S REPORT NUMBER(S)</b>		
<b>12. DISTRIBUTION/AVAILABILITY STATEMENT</b> A DISTRIBUTION UNLIMITED: PB Public Release						
<b>13. SUPPLEMENTARY NOTES</b>						
<b>14. ABSTRACT</b> This project primarily investigated computationally the infusion of liquid elements from the Hf family (i.e., Hf, Ti and Zr) into a capillary to understand the effects of surface tension and viscosity during processing of melts with a packed bed of B4C to form boride-carbide precipitates. Although the ultimate goal of the research endeavor is to enhance significantly the oxidation resistance of ultrahigh temperature ceramic composites (UHTCC), the processing of these reactive metals and non-metals must be improved dramatically to control the eventual development of the oxide scale.						
<b>15. SUBJECT TERMS</b> ceramics, boron, ultra-high temperature						
<b>16. SECURITY CLASSIFICATION OF:</b>			<b>17. LIMITATION OF ABSTRACT</b>  UU	<b>18. NUMBER OF PAGES</b>	<b>19a. NAME OF RESPONSIBLE PERSON</b> Arturo Bronson	
<b>a. REPORT</b>  Unclassified	<b>b. ABSTRACT</b>  Unclassified	<b>c. THIS PAGE</b>  Unclassified			<b>19b. TELEPHONE NUMBER (Include area code)</b> 915-747-6931	

**FINAL REPORT**

**for the**

**Research Project  
(AFOSR Award Number – FA9550-12-1-0242)**

**Entitled**

**Computational – Experimental Processing of Boride/Carbide Composites by  
Reactive Infusion of Hf Alloy Melts into B<sub>4</sub>C**

**By**

**Arturo Bronson and Vinod Kumar  
Department of Mechanical Engineering  
University of Texas at El Paso**

**July 2015**

**Computational-Experimental Processing of Boride/Carbide Composites by Reactive  
Infusion of Hf Alloy Melts into B<sub>4</sub>C  
Arturo Bronson and Vinod Kumar, The University of Texas at El Paso**

**Project Summary**

This project primarily investigated computationally the infusion of liquid elements from the Hf family (i.e., Hf, Ti and Zr) into a capillary to understand the effects of surface tension and viscosity during processing of melts with a packed bed of B<sub>4</sub>C to form boride-carbide precipitates. Although the ultimate goal of the research endeavor is to enhance significantly the oxidation resistance of ultrahigh temperature ceramic composites (UHTCC), the processing of these reactive metals and non-metals must be improved dramatically to control the eventual development of the oxide scale. **The research effort used computational thermodynamics and computational fluid dynamics (CFD) to predict phase equilibria and melt flow into pore channels, respectively, with strategic experimentation** through the following integrated research objectives:

- Investigate the use of surface tensions of liquid Hf, Sm, Ti, Y and Zr to predict their infusion into a B<sub>4</sub>C packed bed by computational fluid dynamics.
- Investigate the extent of reactive infusion with strategic experimentation of liquid Al-Sm alloys containing Hf, Ti or Y.
- Investigate the phases formed as the liquid metal flows into the packed bed of B<sub>4</sub>C.

Although the alloy melt infiltrates as a result of the surface tension, viscosity, the liquid/B<sub>4</sub>C reaction, and the diffusion of components, **the surface tension of the melt serves as the key parameter affecting the depth of melt penetration of liquid elements (i.e., Hf, Sm, Ti, Y and Zr) into pores.**

The research applied computational fluid dynamics (CFD) to simulate the flow characteristics of the melt from the Hf family of elements, as well as Y and Sm, through pore channels. The volume of fluid (VOF) approach with the momentum equations incorporating surface tension and contact angle terms was used to track the interface of fluid penetration into a pore. A pore-network modeling incorporating surface tension terms through contact angle and pore throat/nodes reconstructions is also considered for predicting dispersion.

A modified Semlak-Rhines model was developed for liquid metal penetration into a packed bed and considers the contribution of the forces incorporating surface tension, viscosity, gravity and end-drag. For liquid Ti, the surface tension dominated the capillary flow at small times ( $< 1 \mu\text{s}$ ) with the viscous force having a synergistic effect at longer times ( $> 10^{-4.5} \text{ s}$ ). At small time (i.e.,  $< 1 \mu\text{s}$  range), the penetration rate reaches a maximum in the m/s range at approximately  $1 \mu\text{s}$ , but the rate decreases with increasing time at which the rate of penetration compares favorably with the Semlak-Rhines equation. Though the surface tension is sometimes considered as the driving force in capillary flow, the contribution of the viscosity to the flow may dominate the surface tension-viscosity dissipation as the flow occurs at longer times or achieves a steady-state condition.

Strategic experimentation involved Al-Sm and Al-Sm-Me (Me=Hf, Y or Zr) alloy melts infusing into a B<sub>4</sub>C packed bed at temperatures  $\geq 1973\text{K}$  ( $1700^\circ\text{C}$ ). The fluid dynamics of the Al-Sm-Hf and Al-Sm alloy melts was investigated through varying spatial pore channels and the elemental components formed carbide and boride phases (e.g., Al<sub>3</sub>BC).

## 1. Introduction

Ceramic composites and intermetallics have become the core materials to meet the strength and extreme temperature needed for gas-turbine engines and hypersonic aerosurfaces [1]. The successful integration of an ultrahigh-temperature, ceramic composite (UHTCC) for these applications requires careful and optimal consideration of processing, mechanics and oxidation. The research focuses on predicting the fluid flow of liquid melts from the mainly the Hf family (i.e., Hf, Ti and Zr) into a packed bed of  $B_4C$ . During infiltration, reactions between the alloy melt and  $B_4C$  will form an  $HfB_2$ - $HfC$ /Hf-Y-Ti composite, which will eventually develop an  $HfO_2$ - $Y_2O_3$ - $TiO_2$  scale, as configured in Figure 1. The oxide scale must be configured with precipitates embedded and aligned to minimize the stress/strain distribution, but the key to the configuration is the predictability and control of the fluid flow processing at ultrahigh temperatures. For example, the phase equilibria of the pyrochlore phase (or  $Y_2Ti_2O_7$ ) within an  $HfO_2$ - $Y_2O_3$ - $TiO_2$  scale may form as layers of  $Y_2Ti_2O_7$ ,  $HfTiO_4$ , cubic- $HfO_2$ , or tetragonal- $HfO_2$  as the alloy melt reacts with  $B_4C$ . In addition, accurate chemical behavior of the Hf systems at extreme temperatures is needed to adequately predict performance. The stable and metastable conditions may adjust the final microstructure of the actual oxide interphase protecting the matrix at ultrahigh temperatures.

On a previous study, the computational-experimental approach was used to investigate the effects of thermal mismatch and growth stresses on the  $ZrB_2$ /ZrC/Zr-Si [2] system. However, the operational boundaries must be pushed by using rutile instead of silica to control vaporization [3] and Hf components rather than Zr compounds to attain better ultrahigh temperature performance. In addition, to acquire the ultimate Hf protective-scale system, the processing of the Hf melts with  $B_4C$  must be better controlled. **With an expertise in computational fluid dynamics (Kumar) and in high temperature reactions (Bronson), the collaboration investigated liquid alloy infusing into a packed bed of  $B_4C$ .** However, to improve the characteristics of a boride/carbide system, the research studied the processing science of toward controlling non-reactive infusion into  $B_4C$ .



**Figure 1 -- Oxide Scale developed from the  $ZrO_2$ - $Y_2O_3$ - $TiO_2$  System to protect a boride/carbide/metal matrix**

## 2. Research Effort and Findings

### 2.1. Consideration of Infusion Driven by Surface Tension (or Surface Energy):

The dynamics of liquid metal wetting across surfaces or into porous media encompasses a wide-ranging of material processing (e.g., brazing and reactive infiltration), as reviewed by Delanny et. al [4], Eustathopoulos [5] Saiz and Tomsia [6] and Liquid-metal reactive infiltration offers a methodology for near-net processing of metal or ceramic composites by penetrating liquid metal into a ceramic preform (e.g., Al into mullite [7] or Zr into  $B_4C$  [8]). Although originally elemental liquids of Hf, Ti and Zr were infused into  $B_4C$ , as reported by Johnson, Nagelberg and Breval [8] for liquid Zr, more recently Maheswaraiah, Sandate and Bronson [9] studied the infusion of a liquid Zr-Si alloy with  $B_4C$  to form ZrC and  $ZrB_2$  precipitates embedded within a Zr-Si matrix. To optimize the processing, a better understanding of the infusion of

liquid metal into a ceramic preform is needed to predict and to design ultimately the metal matrix composites or ceramic matrix composites.

The dynamics of wetting for liquid metals on surfaces differ from organic liquids because the interfacial energies of the former are greater than the latter, as noted by Saiz and Tomsia [10]. A consequence of the interfacial energies is the significant spreading rates of liquid metals on metals and nonmetals. For example, Saiz, Hwang, Suganuma and Tomsia [11] determined that the spreading rates of Sn-Ag solders at a temperature of 723 K (996°C) after contacting Fe-42 Ni  $pO_2 < 10^{-19}$  kPa. Also, Grigorenko, Poluyanskya, Eustathopoulos and Naidich [12] reported spreading velocities of 0.5 to 1 m/s for Ni and NiPd melts on  $\alpha$ -SiC, as well as NiPdTi and CuSnTi melts on vitreous carbon, at 1473-1773 K (1200-1500°C) in a vacuum. The dynamics of wetting of liquid metals may incorporate the effects of surface tension, adsorption of active species, and interfacial reaction though the mechanistic explanations have evolved from the use of a force balance in the Young equation as explained by Lupis [13] to applying the molecular-kinetic theory such as Benhassine [14] for Cu-Ag melts on Ni surfaces and Swiler and Loehman [15] for reactive surfaces of the Al-O system. A stochastic mathematical framework was investigated by Delgado and Kumar [16] to investigate the effects of heterogeneity in the pore-structure. Delgado and Kumar also investigated a multiscale approach to couple the micro (pore) - physics with the macroscale investigation [17].

To predict the fundamental concepts involving the fluid flow of liquid metal driven by surface tension into a porous structure of a packed bed, Semlak-Rhines [18] developed expressions assuming flow through capillary parallel tubes. Martins, Olson and Edwards [19] analyzed the Semlak-Rhines expressions and selected an infiltration rate parameter consisting of the surface tension-force to viscosity ratio independent of the liquid density for evaluating the effect of alloy composition on the flow into porous media.

Although the dynamics of reactive wetting would fundamentally incorporate the mechanisms noted previously, and even the effects of a temperature spike from exothermic interfacial reactions, the fluid flow into the packed must be understood first to determine the differential between non-reactive and reactive wetting kinetics. Hence, the primary purpose of the present study was to determine the fluid flow driven by the surface tension-viscosity dissipation as the liquid metal penetrates into the pores of a ceramic preform. The present study focused on the surface tension-viscosity dissipation assuming an unreactive pore surface, and left the dynamics of reactive wetting of a ceramic substrate for future work.

## 2.2 Theoretical Basis

The starting equation is given by conservation of momentum equation in the axial direction for a capillary, as given by Semlak and Rhines [18], a modified form of the differential equation by Ligenza and Bernstein[20], assumes rapid wetting without any reaction between the liquid and solid and is given as follows:

$$\begin{aligned} \frac{d}{dt} \left( \pi R^2 [\rho h + \rho_g (l - h)] \frac{dh}{dt} \right) = 2\pi R \sigma \cos(\theta) - 8\pi \left( \frac{dh}{dt} \right) (\mu h + \mu_g (l - h)) \\ - \pi R^2 g h (\rho - \rho_g) - \frac{1}{4} \pi R^2 \rho \left( \frac{dh}{dt} \right)^2 \end{aligned} \quad (1)$$

The rate of momentum accumulation on the left side of the equation equals the summation of the forces on the right side for the terms involving surface tension ( $\sigma$ ) with the contact angle ( $\theta$ ),

viscosity ( $\mu$ ), gravity and the end-drag, respectively. For the simplified case, assuming gas density ( $\rho_g$ ) and viscosity ( $\mu_g$ ) are negligible, Eq. (1) becomes

$$\rho \frac{d}{dt} \left( \pi R^2 h \frac{dh}{dt} \right) = 2\pi R \sigma \cos(\theta) - 8\pi \mu h \left( \frac{dh}{dt} \right) - \pi R^2 g h \rho - \frac{1}{4} \pi R^2 \rho \left( \frac{dh}{dt} \right)^2 \quad (2)$$

When the fluid flow in the capillary has fully developed which can occur at sufficiently small times, the rate of rise is being slowed enough that the rate of change of momentum and the end-drag  $R\sigma\cos\theta/2\mu$  and rate of penetration,  $dh/dt = R\sigma\cos(\theta)/4\mu t$  as developed by Semlak and Rhines[18]. However, Eq. (2) does not result in explicit solution when  $t \rightarrow 0$  when the mass entered in the capillary tube and its velocity is zero. The surface tension term is assumed constant and independent of the depth of penetration of the liquid in the tube. This implies that, for the right hand of the Eq. (2) to be constant, the liquid must accelerate at infinite acceleration.

To address the singularity, we assume that the meniscus has already been formed as shown in the Figure 2. The height ( $h$ ) of the meniscus in Eq. (2) can be separated into two terms,  $h$  and  $h_0$ . The modified Eq. (2) becomes

$$\begin{aligned} \frac{d}{dt} \left( (\rho\pi R^2 h + \rho V_L) \frac{dh}{dt} \right) &= 2\pi R \sigma \cos(\theta) - 8\pi \mu (h + h_0) \left( \frac{dh}{dt} \right) \\ &\quad - \rho(\pi R^2 h + V_L)g - \frac{1}{4} \rho \pi R^2 \left( \frac{dh}{dt} \right)^2 \end{aligned} \quad (3)$$

$V_L$  is the liquid volume bounded by the horizontal plane passing through the lowest point of the fluid surface and the plane containing the contact line, and  $h_0$  is the maximum height of the liquid above the lowest point of the liquid surface for the contact angle  $\theta$ . The initial conditions are as follows:

$$h|_{t=0} = 0; \quad \left. \frac{dh}{dt} \right|_{t=0} = 0 \quad (4)$$

### 2.3 Results of Applying Liquid Elemental Properties from the Ti Family, Y and Sm to Modified Semlak-Rhines (SR) Equation:

For liquid Ti flowing into a capillary with a 10  $\mu\text{m}$  diameter, the velocity was calculated by using the Semlak-Rhines (SR) equation (i.e., Eq. 2) and compared with the modified-SR equation incorporating the inertia and end-drag terms, as shown in Figure 3. The thermophysical properties were acquired from the recent review of Paradis et al. [21] and the viscosity value from Ishikawa et al.[22] who updated the measured data measured primarily with electrostatic levitation, a containerless experimental method. The melting temperatures were the same as reported by Massalski et al. [23] except for yttrium. Paradis, Ishikawa and Koike [24] reported a yttrium melting of 1796 K (1523°C) as compared with the yttrium phase diagrams (e.g., Ti-Y) depicting a melting temperature of 1795 K (1522°C) though the temperature differential is within the error of the measured physical properties. The viscosity data was extrapolated to 2573 K (2300°C) for comparison of the velocity of liquid moving into the capillary at an isothermal temperature of the elements.

The velocity was calculated at the melting temperature of Ti. For times greater than 10  $\mu\text{s}$ , both equations give similar velocities. However, for times less than 10  $\mu\text{s}$ , the SR velocity of the liquid infusion into the pore increases significantly and unrealistically, but the modified-SR velocity plateaus at 7 m/s and then decreases with decreasing time (as seen in the Figure 3). In the modified-SR equation, it is observed that all surface tension force is being used to accelerate

the mass (inertia) in the capillary as the time approaches zero. The relative importance of each term in Eq. (3) with decreasing time can be more easily compared by dividing each term by the surface tension term (i.e.,  $2\pi R\sigma\cos(\theta)$ ). At  $t=10^{-7}$  s, the inertia term (or the left side of Eq. (3) indicating the summation of the forces on the right side becomes driven by the surface tension, as shown in Figure 4. The inertia term was not present in the standard SR equation resulting in a singularity.

The surface tension force contributes towards accelerating the fluid, and quickly reduces to zero at around 10  $\mu$ s as the end-drag (which is proportional velocity squared) quickly becomes significant. The end-drag term reaches a maximum at around the same time and accounts for  $F_{drag}/F\sigma = \sim 0.9$ . The maximum velocity is also achieved at this time. The viscous term (which is proportion to the velocity as well as the depth of penetration) slowly becomes more important. Since the drag and viscous forces act as resistance and as more liquid enter the capillary, the viscous force increases, the liquid starts slowing down reducing in the drag force faster than the viscous terms. This results in slight increase in the inertia term peaking at around 50  $\mu$ s. After this, the viscous term becomes significantly more important than the drag or the  $F_{viscous}/F\sigma \sim 1 \gg F_{drag} \text{ or } inertia/F\sigma$  ) resulting an approximation similar to SR (as supported by Figure 4).

## 2.4 Discussion of Results Acquired from Modified Sendlak-Rhines (SR) Equation

The effect of the contact angle and surface tension on the maximum calculated velocities was evaluated further to determine the major parameter driving the infiltration of the elemental liquid metal into the pore. The contact angle of the liquid Ti meniscus on the inner wall of the capillary also has a significant effect on the velocity, as shown in Figure 5. The maximum velocity of the liquid Ti at its melting temperature decreases from 7 to 2.7 m/s for a contact angle increasing from  $0^\circ$  to  $80^\circ$ , respectively. Though liquid Ti penetration initially approaches greater than 1 m/s, the velocity of infusion appears to decrease asymptotically to less than 0.1 m/s with increasing times greater than a ms. However, Eq. (3) does not account for variation in the contact angle, which can change significantly as the liquid metal reacts with the surface and as Loehman, Ewsuk and Tomsia [7] and Saiz et al. [10] have reported. The transient effect of the contact angle on the velocity of penetration is beyond the scope of this paper though the reactive wetting of the surface should consider the interfacial kinetics.

The velocities of liquid Ti, Y, Hf, Zr and Sm were also determined with the modified-SR equation at their respective melting temperatures, as shown in Figure 6. For the group IV elements (Ti, Zr and Hf), their velocities especially the maximum velocity increases with the decreasing order of the atomic weight, but the trend does not follow with the inclusion of Y and Sm. The maximum velocity increases with increasing surface tension of Sm, Y and Ti, as shown in Table 1. However, the surface tensions for Ti and Zr have very similar values (Table 1) with only a  $\Delta\sigma$  of  $0.1 \text{ Nm}^{-1}$ , but the respective velocities differ with the differential,  $\Delta v_{max}$ , approximating 1 m/s. In addition, the Hf velocity with surface tension does not follow the increasing trend. The maximum velocity for Hf, Ti, Y and Zr were also calculated at a constant temperature of 2573 K (2300°C), but a similar behavior was observed without an increasing trend as shown in Table 2.

The effect of the surface tension to viscosity ratio on the maximum calculated velocity was also evaluated, but does not have a trend at the melting temperature, as evident in Table 1. The synergistic effect of the surface tension and viscosity depends on the transient time, as



shown in Figure 5. However, in examining the terms of the forces (Figure 4), the ratio of the viscous to surface tension forces increases with increasing time. At an isothermal temperature of 2573 K (2300°C), the surface tension to viscosity dissipation (or ratio,  $\sigma/\mu$ ) does indeed have a trend decreasing with increasing elemental melting temperature. Though the surface tension is sometimes considered as the driving force in capillary flow, the contribution of the viscosity to the flow may dominate the surface tension-viscosity dissipation as the flow occurs at longer times or achieves a steady-state condition.

## **2.5 Conclusions from the Computational Analysis of Capillary Flow**

The surface tension-viscosity dissipation driving the fluid flow within a capillary, the high-temperature liquid metal infusion was analyzed for titanium, yttrium, hafnium and zirconium to predict their penetration into a packed bed. A model of the dissipation considered the momentum balance within the capillary to determine rate of infusion, which modified the Semlak-Rhines model developed for liquid metal penetration into a packed bed assumed as a bundle of tubes mimicking the porosity of a packed bed. The modified model considers the contribution of the forces incorporating surface tension, viscosity, gravity and end-drag. For liquid Ti, the surface tension dominated the capillary flow at small times ( $< 1 \mu\text{s}$ ) with the viscous force having a synergistic effect at longer times ( $> 10^{-4.5} \text{ s}$ ). At small time (i.e.,  $< 1 \mu\text{s}$  range), the penetration rate reaches a maximum in the m/s range at approximately  $1 \mu\text{s}$ , but the rate decreases with increasing time at which the rate of penetration compares favorably with the Semlak-Rhines equation. Though the surface tension is sometimes considered as the driving force in capillary flow, the contribution of the viscosity to the flow may dominate the surface tension-viscosity dissipation as the flow occurs at longer times or achieves a steady-state condition.

**Table 1-Physical Properties at Melting Temperature of Liquid Elements**

Element	Melting Temperature K (°C)	Surface Tension ( $\sigma_{mp}$ ) $\text{Nm}^{-1}$	§Viscosity ( $\mu_{mp}$ $10^3$ ) $\text{kgm}^{-1}\text{s}^{-1}$ (Pa•s)	Density ( $\rho_{mp}$ $10^{-3}$ ) $\text{kgm}^{-3}$	$\sigma_{mp}/\mu_{mp}$ $\text{ms}^{-1}$
Hafnium	2504 (2231)	1.612	7.1	11.82	227
Titanium	1941 (1668)	1.555	3.3	4.17	471
Samarium	1347 (1074)	0.430	2.29	7.02	188
Yttrium	1795 (1522)	0.804	4.54	4.15	177
Zirconium	2128 (1855)	1.464	4.74	6.21	316

\*Thermophysical data were acquired from Paradis et al.[21].

§Viscosity values were extrapolated from experimental data of Ishikawa, Paradis, Okada and Watanabe [22].

**Table 2-Physical Properties of Liquid Elements at 2573 K (2300°C)**

Element	Surface Tension ( $\sigma$ ) $\text{Nm}^{-1}$	§Viscosity ( $\mu$ ) $10^3$ $\text{kgm}^{-1}\text{s}^{-1}$ (Pa-s)	Density ( $\rho$ ) $10^{-3}$ $\text{kgm}^{-3}$	$\sigma/\mu$ $10^{-3}$ $\text{ms}^{-1}$
Hafnium	1.60	6.69	11.8	239
Titanium	1.44	2.16	4.03	667
Samarium	0.341	N/A	N/A	
Yttrium	0.765	0.491	3.99	1558
Zirconium	1.41	3.00	6.09	483

§Viscosity values were extrapolated from experimental data of Ishikawa, Paradis, Okada and Watanabe [22].

**Table 3: List of Symbols and Their Units**

Parameter Description	Symbol	Unit
Capillary Radius	$R$	m
Temperature	$T$	K (°C)
Liquid Viscosity	$\mu$	Pa-s
Surface Tension	$\sigma$	N/m
Liquid Density	$\rho$	$\text{Kgm}^{-3}$
Contact Angle	$\theta$	Degrees
Acceleration Due to Gravity	$g$	$\text{ms}^{-2}$
Height of lowest point from the liquid curved surface	$h$	m
Height of the liquid above the lowest point of the liquid surface	$h_o$	m
Equilibrium Capillary Rise Height	$h_e$	m
Non-Dimensional Viscosity	$\tilde{\mu}$	-
Non-Dimensional Liquid Volume Above Lowest Point of Liquid Interface	$\tilde{V}_L$	-
Parameter $\alpha = (R/h_e)\tilde{V}_L$	$\alpha$	-

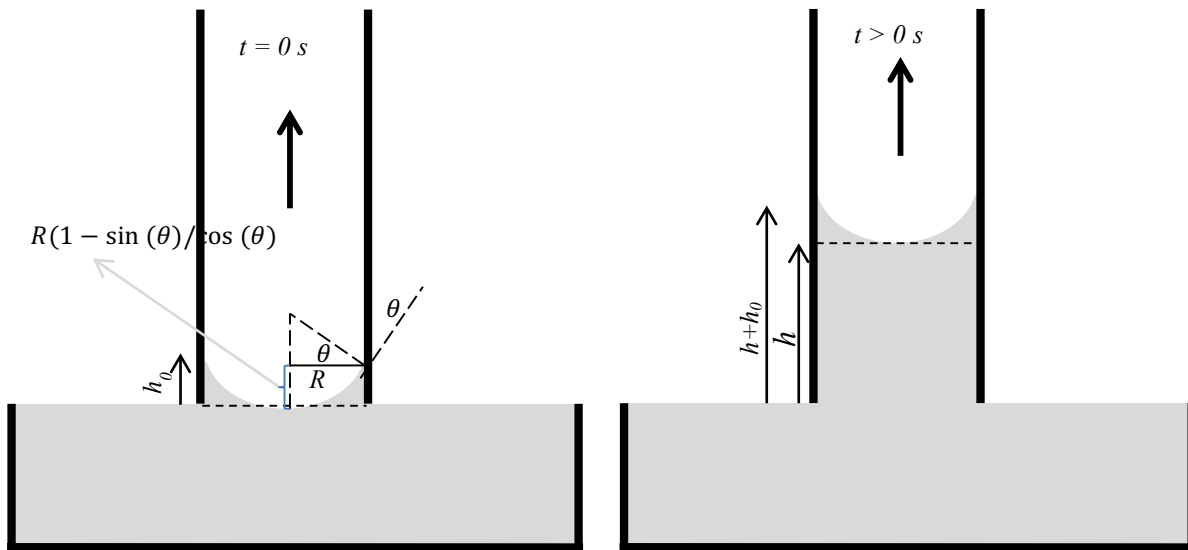


Figure 2 -- Capillary tube is lowered onto the surface of a liquid that wets the tube. (Left) Liquid interface arranges to equilibrium capillary shape when the bottom of the tube contacts the liquid. (Right) Liquid moves into tube under the influence of capillary forces

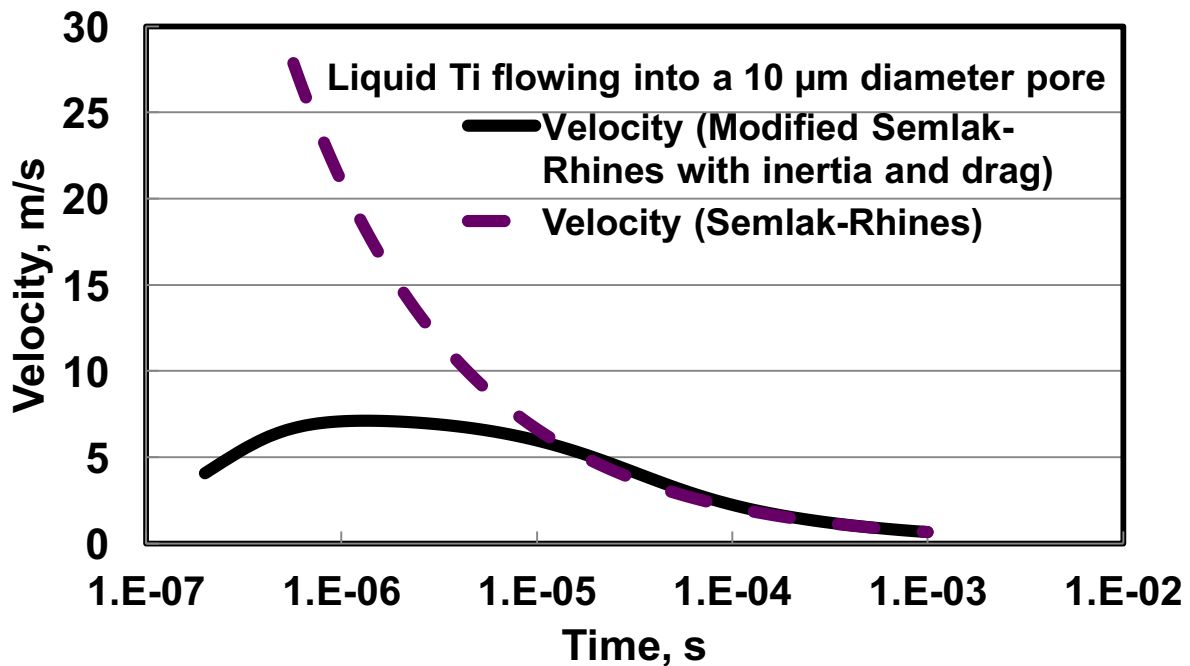


Figure 3 -- Calculated velocity determined by the Senglak-Rhines equation at the melting temperature of 1941 K (1668°C) for liquid Ti with and without the inertia and end-drag consideration.

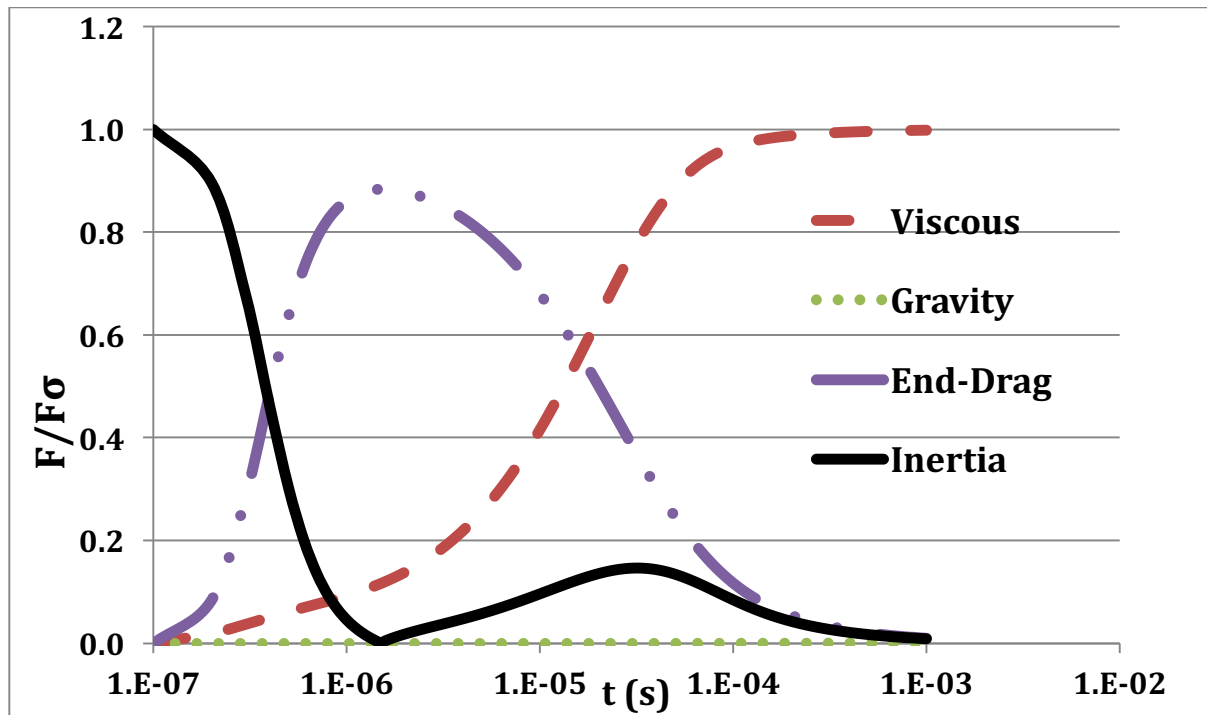


Figure 4 -- Importance of the various terms in Eq. (1) with respect to surface tension ( $F_\sigma$ ).

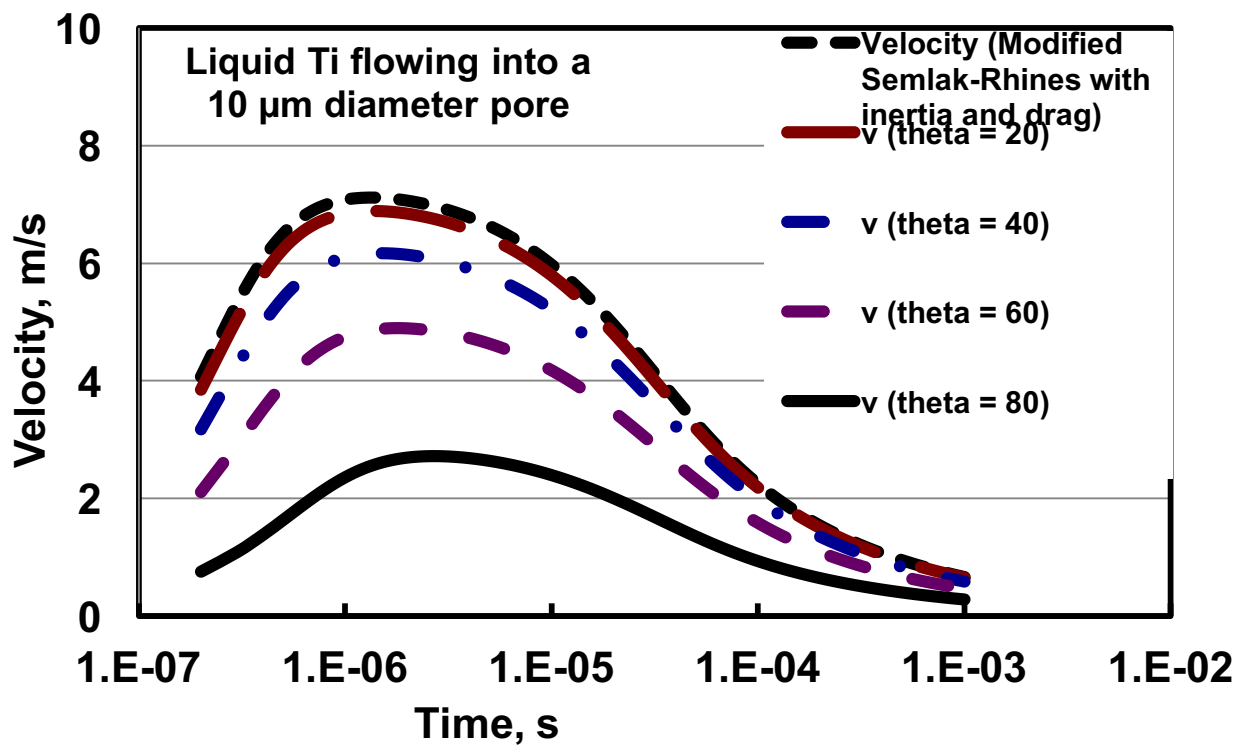


Figure 5 -- The effect of the contact angle ( $\theta$ ) on the calculated velocity ( $v$ ) using the modified-SR equation for liquid Ti at 1941 K (1668°C) flowing into a 10  $\mu\text{m}$  diameter pore.

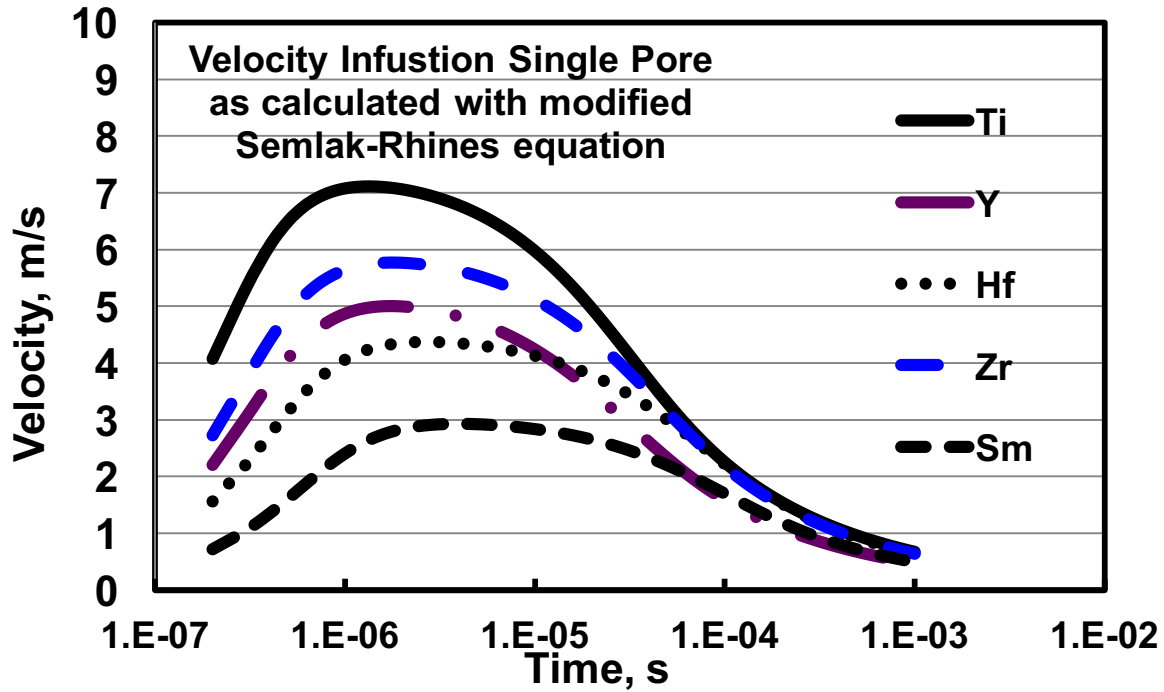


Figure 6 -- Velocity of elemental liquid for Ti, Y, Hf, Zr and Sm calculated with the modified-SR equation at their respective melting temperature.

## 2.6 The capillary infusion into a pore calculated by computational fluid dynamics simulations compared to the Semlak-Rhines Equation

For an understanding of the infusion of liquid hafnium ( $Hf_L$ ), which simultaneously reacts with the packed bed of  $B_4C$ , the present study approaches the behavior from the effect of surface tension or surface energy. The surface related parameters should examine the thermodynamic approach and Navier-Stokes approach though the thermocapillary effect (or Marangoni forces) should also be incorporated, because the exothermic  $Hf_L/B_4C$  reaction increases the temperature sometimes by  $200^\circ C$ . For a synopsis presented here, the surface tension and energy is explained with the effects of the fluid dynamics on the infusion.

The Young-Dupré equation, which considers the forces acting on the point of intersecting lines for the solid/gas ( $\sigma_{sg}$ ), liquid/solid ( $\sigma_{ls}$ ), and liquid/gas ( $\sigma_{lg}$ ) interfaces, acquires the surface tension as explained by Lupis [13] and Gallois and Lupis [25] by measuring the contact angle, as depicted in Figure 7 and the following equation:

$$\sigma_{sg} = \sigma_{ls} + \sigma_{lg} \cos \theta \quad (1)$$

For two fluids (i.e., liquid and gas or two liquids), the force of the interface created with the solid and liquid minimizes the free surface energy by decreasing the surface area, as shown in Figure 7.

Infusion of Hf-Y-Ti melts through a

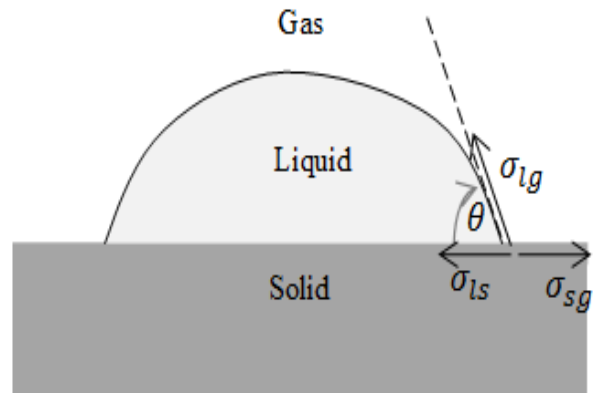


Figure 7 -- Sketch of contact angle resulting from forces

B<sub>4</sub>C packed bed heavily depends on surface and interfacial tensions of the liquid alloy with the gas/solid surfaces and solid surfaces, respectively, as the liquid alloy permeates the pores via capillary flow, reacts with B<sub>4</sub>C to form HfB<sub>2</sub> and HfC with any remaining Hf alloy melt exposed to a temperature gradient. Although the term of surface tension ( $\sigma$ , work/area), or work required to change the interface by a unit area, as defined by Wagner [26] has been used, one should note that Hondros [27] differentiates between surface energies (e.g., mJ/m<sup>2</sup>) and surface tensions (e.g., mN/m). Lupis [13] also uses surface tension (force/length) though simply multiplying and dividing a length unit relate the energy and force terms, which are henceforth distinguished by  $\sigma^A$  and  $\sigma^F$ , respectively. The effects of surface adsorption on the thermodynamic stability is developed from the Gibbs free energy,  $G$ , as reported by Wagner [26].

$$dG = -SdT + VdP + \sigma dA + \sum \mu_i dn_i \quad (2)$$

where symbols represent the usual terms such as entropy ( $S$ ), volume ( $V$ ), surface tension ( $\sigma$ ) and chemical potential ( $\mu$ ). The oxygen potential would affect the adsorption in a thermodynamic system and related according the following equation derived from Eq. (2):

$$\Gamma_o^{Hf} = -\frac{1}{RT} \left( \frac{\partial \sigma^A}{\partial \ln p_{O_2}} \right)_{T, i \neq k} \quad (3)$$

$\Gamma(OHf)$  would have a significant effect on the surface energy ( $\sigma^A$ ), especially since oxygen dissolves significantly in pure Hf.

The research effort simulated the infusion into a pore by using computational fluid dynamics with Fluent software and compared its results with the Semlak-Rhines infusion equation [18] to acquire the depth of infusion ( $d$ ) related by  $\sigma^F$  as follows:

$$d = \left[ \frac{R\sigma^F t \cos\theta}{2\eta} \right]^{0.5} \quad (5)$$

They derived the equation for a liquid rising into straight capillary tubes of radius ( $R$ ), with a contact angle ( $\theta$ ), the viscosity ( $\eta$ ) of the liquid. The depth of infusion increases with decreasing contact angle, but it appears to have a minimal effect with contact angles less than 20°, as shown in 4.

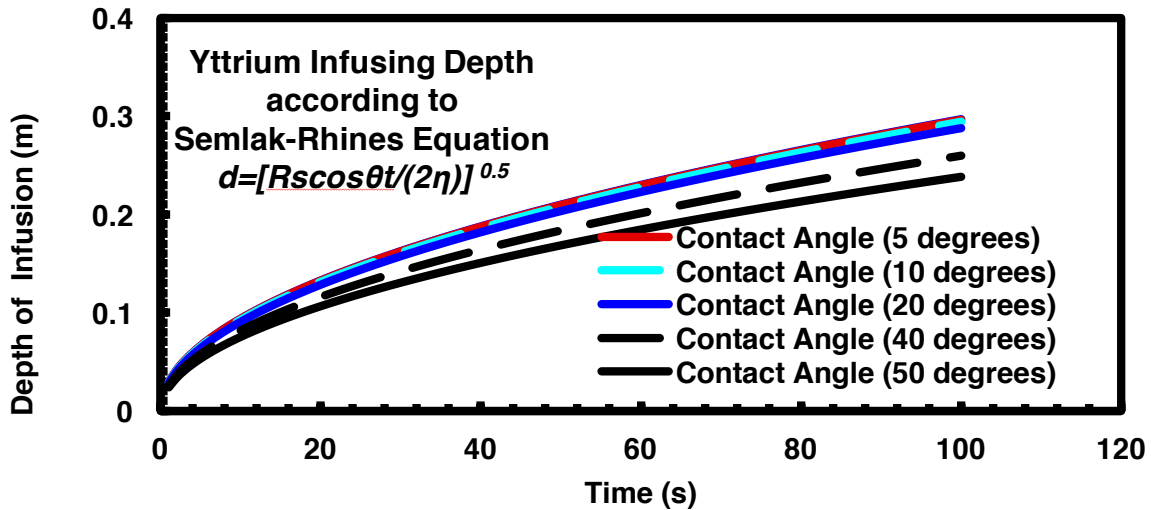


Figure 8 -- Depth of infusion of liquid yttrium according to the Semlak-Rhines equation

The Fluent software was configured to have volume elements simulating liquid hafnium (i.e., 0.1 mm x 0.1mm with 49,284 elements), liquid yttrium, or liquid titanium above a solid matrix containing one pore, as shown in Figure 9. A pore size had a 10 $\mu$ m diameter and 1mm deep with 244,442 elements. A gas phase of CO maintained at one atmosphere (100 kPa) was also configured beneath the bottom of the pore, though as a fluid CO or air are approximately equivalent. Above the liquid, the pressure of the system had a zero  $\Delta P$  and negating the gravity parameters to simulate the flow.

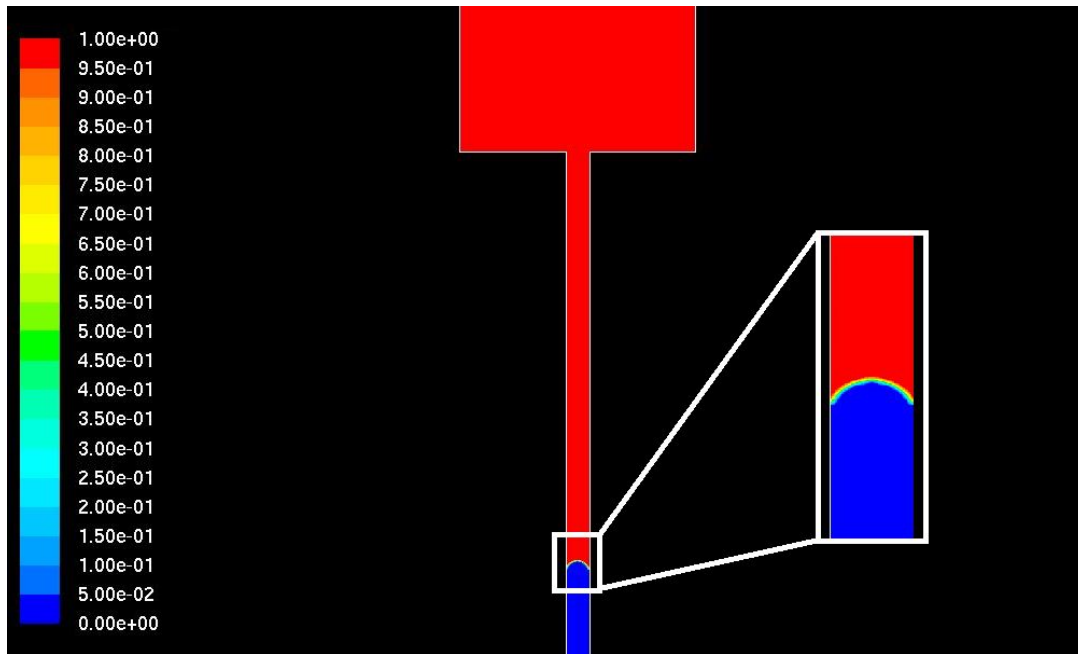


Figure 9 -- Yttrium/CO volume fraction interface in a single pore using fluent

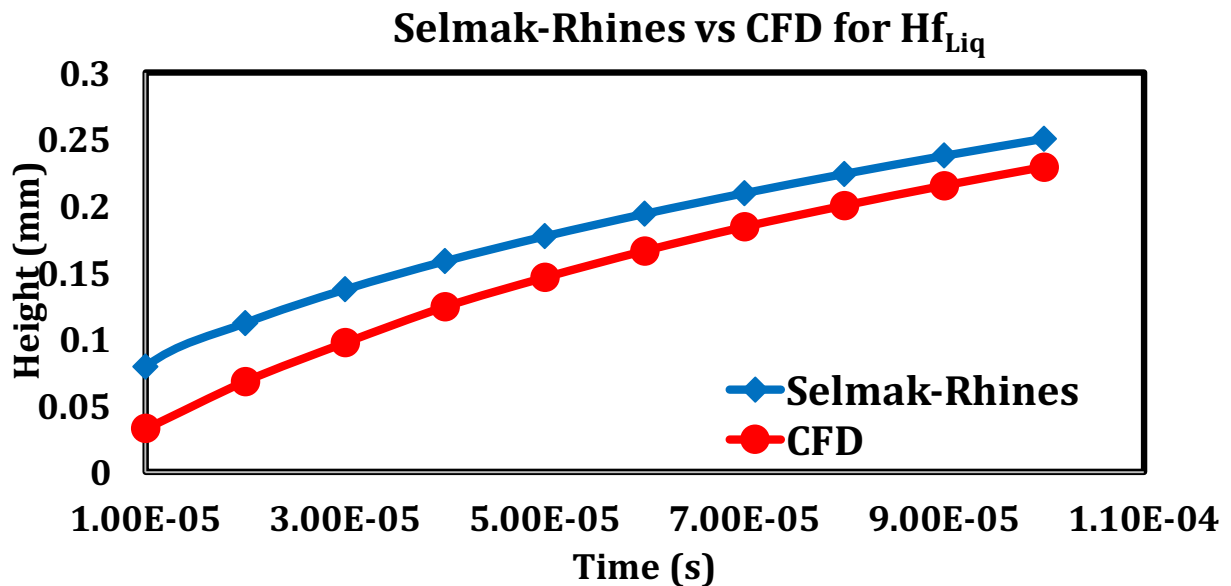
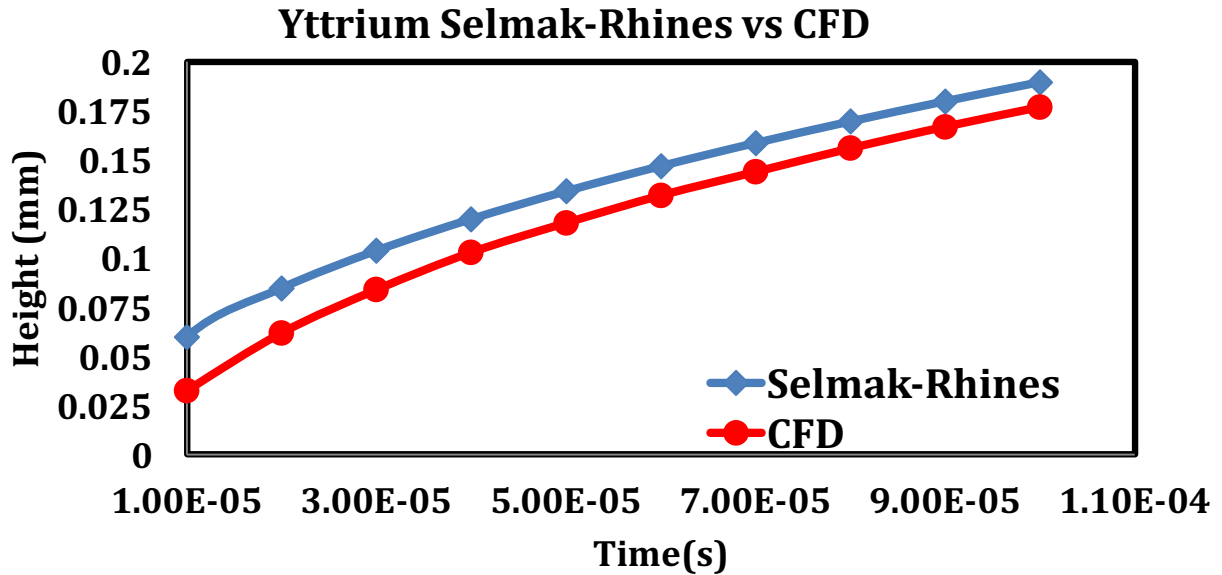


Figure 10 -- Selmak-Rhines vs CFD for Hafnium Penetration

The depth of infusion calculated according to CFD simulation is compared with the Selmak-Rhines equation for liquid Hf at contact angle  $10^\circ$ , as shown in Figure 10. The corresponding calculations for liquid Y and Ti at contact angles of  $10^\circ$  are shown in Figure 11 and Figure 12 respectively. For the liquid Hf simulations from Fluent, the trends are consistently below the Selmak-Rhines calculation though the trends seem to be converging as the time is increasing. The reasons for difference in the depth of infusion may result from the modeling parameters used in the Fluent software. Also, the assumptions made within the Selmak-Rhines equation can take an account for the differences in depth of infusion. We are also currently working on performing the grid-independence study. However, the Selmak-Rhines calculation indicates that the depth of infusion increase dramatically with a contact angle of  $10^\circ$  which is expected.



**Figure 11 -- Selmak-Rhines vs CFD for Yttrium Penetration**

For the infusion of liquid Y with a contact angle of  $10^\circ$ , the CFD simulations seem to correlate with the Selmak-Rhines equation as shown in Figure 11 as time progresses though the pore. Again, the CFD simulations remain in the same range of penetrating depth into the pore. However, the Selmak-Rhines equation does predict as expected, the deepest penetration of the three liquid metals is hafnium due to the ratio of surface tension to viscosity. In addition, all the times were calculated for very brief moments of infusion and simulations are expected for longer times. A similar result was acquired for a Ti melt flowing into a  $10\mu\text{m}$  pore capillary as shown in Figure 12.

The rate of penetration is calculated from the Selmak-Rhines equation and is evaluated as a function of temperature after a specific time,  $100\ \mu\text{s}$ , as shown in Figure 13. Each line represents a different size diameter of the pore. The rate of penetration prediction through the derived equation of Selmak-Rhines equation increases as the temperature increases and is consistent with the varying pore size.

Flow through pore-network was modeled by solving a system of linear equations obtained from the conductance law (mass-conservation principle) at each node for all connected networks using quasi-steady state flow approximations. Conductance of irregular cross-section pore-geometry in Stoke problem is approximated by variation calculus. The basic idea of this variation method is to guess a test velocity function, which satisfies the given no-slip boundaries



conditions. This test function consists of parameters, which are determined by minimizing a functional that represents the total potential energy of the flow field. The resulting velocity function is the approximation to the exact solution of the Stoke equations by the variational method.

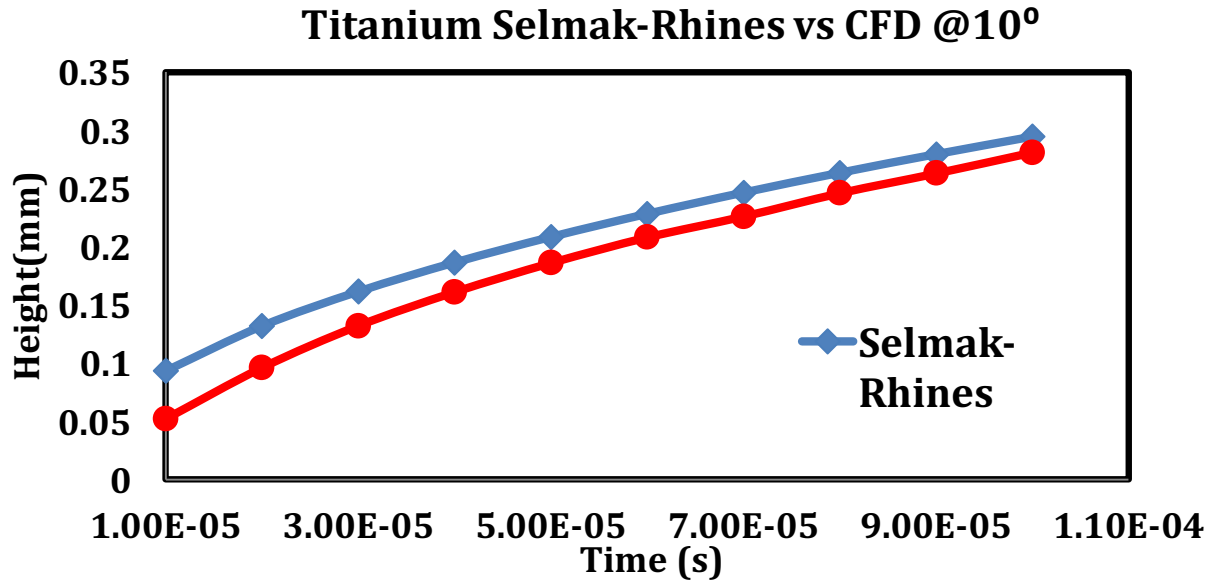


Figure 12 -- Selmak-Rhines vs CFD for Titanium Penetration

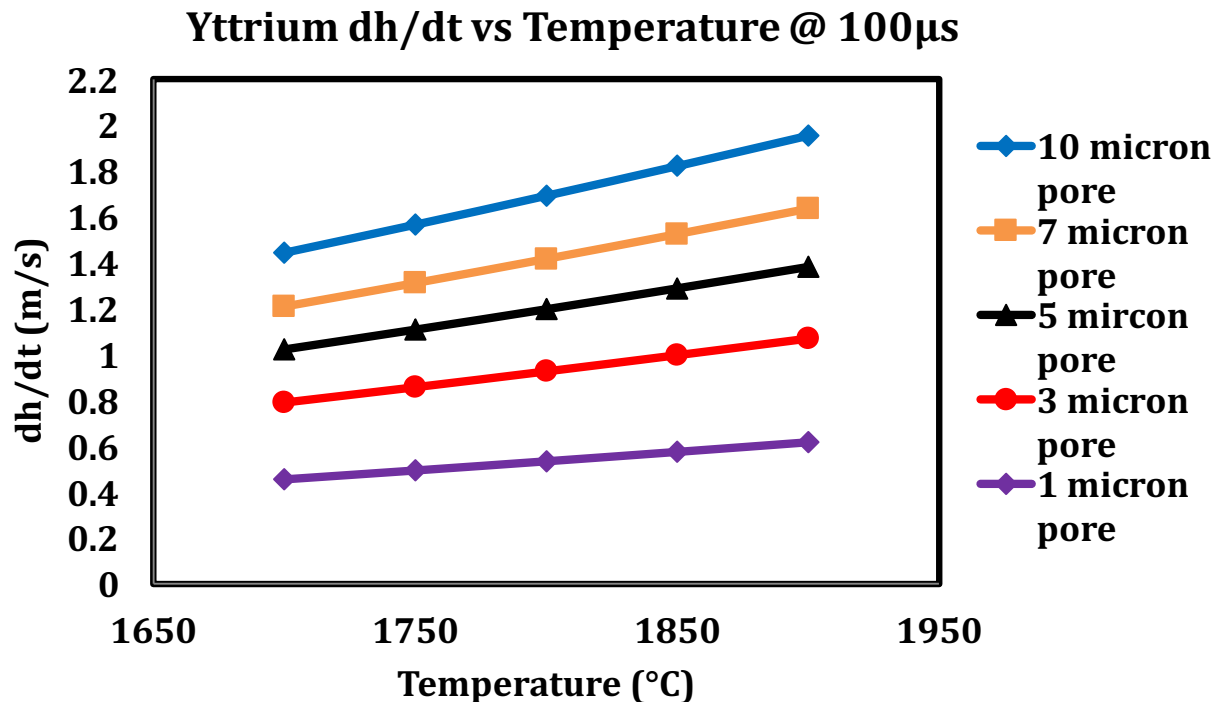
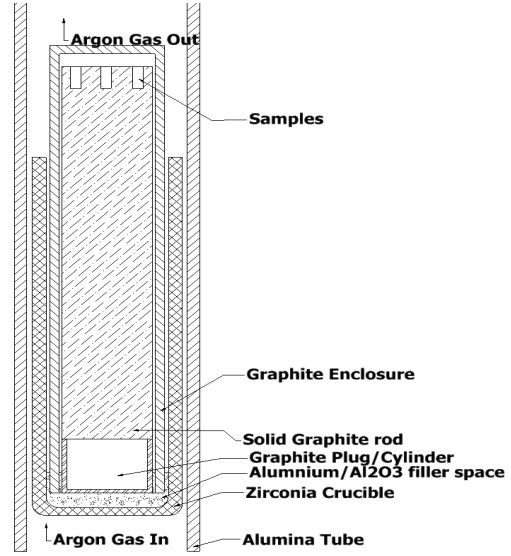


Figure 13 -- Effect of temperature on the calculated rate of penetration yttrium for constant pore size.

**2.7 Experimental Study on the Infusion of Liquid Al-Sm, Al-Sm-Me and Hf-Y-Ti alloys into  $B_4C$ :** The previous processing technique of infusing liquid Zr-Si alloys into  $B_4C$  was changed to study Hf-Y-Ti melts and Al-Sm-Me (Me = Hf, Ti, or Zr) melts into a  $B_4C$  packed bed. A graphite enclosure was used for the processing of the composite, as shown in Figure 14. The samples were placed at the top part of the graphite crucible packed with a  $B_4C$  bed maintained in the hot zone of the furnace (i.e., 1750°C). If needed, the hot zone could have two layers of crucibles with each layer having four crucibles containing the liquid alloy above the  $B_4C$  packed bed. The CO generated from the residual oxygen within the enclosure will serve as a carrier gas pulling oxygen from the hot zone to the cold zone to maintain the oxygen potential of the Al-C-O system. The oxidation potential as determined by Maheshwaraiah, Sandate and Bronson [9] was controlled by liquid Al from 600°C to 1000°C with less vaporization of Al. Aluminum which melts at 661°C and rests at the bottom of  $ZrO_2$ - $Y_2O_3$  crucible within which the graphite enclosure was located.



**Figure 14 -- Sketch of graphite enclosure used to experimentally infuse Hf-Y-Ti melts into  $B_4C$**

Towards the bottom was the zone where the Al melt was placed to seal the crucible thus controlling the oxidation potential within the graphite enclosure serving as closed thermodynamic system. For example, the oxidation potential of  $10^{-47}$  atm will be fixed at the triple point of Al/ $Al_2O_3$ / $Al_4CO_4$ , as shown in Figure 15. To minimize the oxidation of the graphite, deoxidized

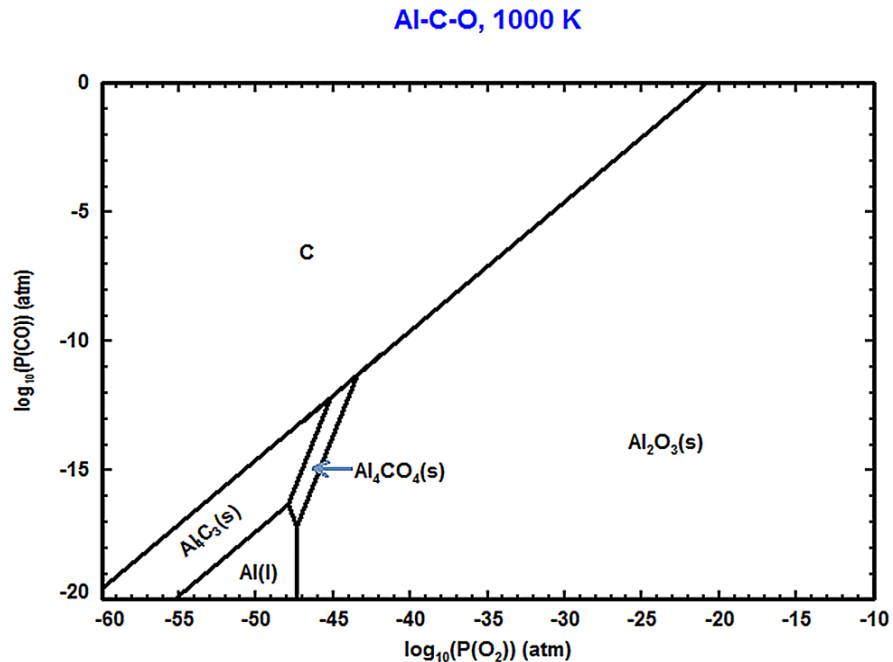


**Figure 15 – Stability diagram for a Al-C-O system**

Ar gas was passed through the alumina tube and subsequently bubbled through dibutyl phthalate to isolate the graphite from the air. The flow rates for the argon gas were measured with a flow meter with an accuracy of  $\pm 1$  mL.

Temperatures were measured with two Pt-20 wt% Rh/Pt-40 wt% Rh thermocouples with the bead located on the inner sidewall of the MoSi<sub>2</sub> furnace chamber though another similar thermocouple was used to determine the temperature profile of the alumina tube containing the graphite enclosure shown in Figure 14.

A major problem in the experiments was the disintegration of the sample by moisture reacting with the yttrium carbide. Although we attempted to determine a method for the formation of YB<sub>2</sub> or even YB<sub>4</sub>, the yttrium composition must be decreased to minimize YC or YC<sub>2</sub> formation. Master Ti-Y-Hf alloy melts were first prepared with compositions as indicated with X marks shown in Figure 16. The compositions chosen for experimentation marked on the red line (Figure 16) lie on the 70 at. % line for Ti content.

For processing with Hf, Ti, Y and Zr alloys, the oxygen potential must be controlled as evident in the stability diagrams for the Ti-C-O and Y-C-O systems superimposed in Figure 18. Yttrium and Ti oxidize to form Y<sub>2</sub>O<sub>3</sub> and TiO at approximately 10<sup>-24</sup> and 10<sup>-19</sup> atm, respectively.

The thermodynamic calculations for the present study were determined with FactSage software and database (version 6.4). The pseudo-isopiestic technique successfully reacted the liquid alloys of the Ti family (i.e., Ti, Hf, and Zr) and Al-Sm system without oxidation, as evident from the microstructures without the formation of oxides (Figures 21 and 26) in the next section.

Although the velocity of liquid Ti, Hf and Zr infusing into a capillary were calculated by the concepts of fluid mechanics according section

2.4, above, the experimental findings determined that a critical parameter needing further study is the contact angle. The liquid alloy must infuse the porous morphology of the B<sub>4</sub>C packed bed shown in Figure 17. Liquid alloys of Hf-Ti-Y were placed on a B<sub>4</sub>C packed bed and even substituting Sm for Y as a component, but the liquid did not penetrate into the pores of the packed bed at 1973 K (1700°C) and sometimes the reaction reaching a temperature greater than

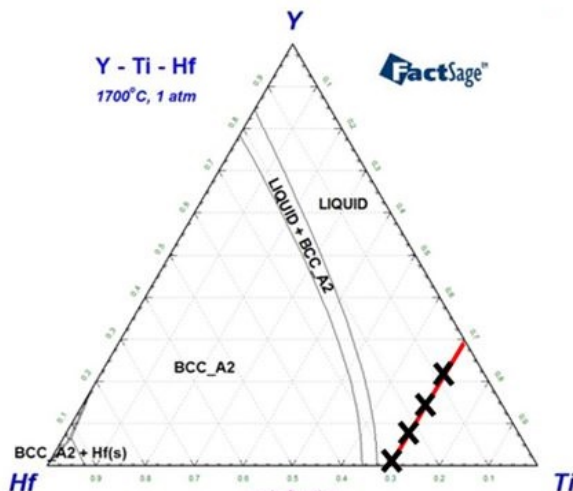


**Figure 16 -- Compositions of master alloys shown on the Hf-Y-Ti phase diagram.**

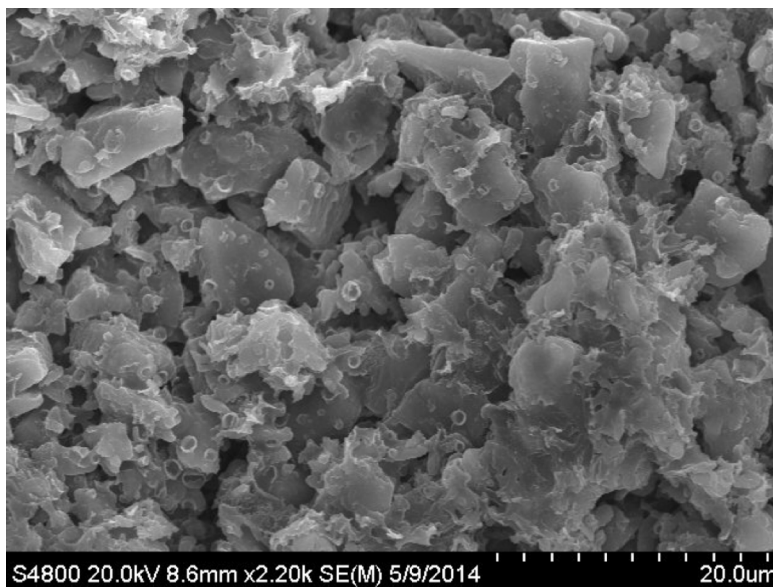


**Figure 17 -- SEM image of pore morphology of B<sub>4</sub>C packed bed**

2045 K (1772°C) as evident from Pt melting and placed adjacent to the graphite crucible containing the Ti-Y-Hf liquid on a B<sub>4</sub>C packed bed. The Hf-Ti-Y calculated phase diagram and the microstructure of Figures 16 and 21 respectively, indicated that a liquid was possible but none of the liquid alloys shown in the Ti-Hf-Y ternary system infiltrated into the B<sub>4</sub>C.

The alloy system was changed to the Al-Sm-Me (with Me = Y, Ti, Hf and Zr) to decrease the melting temperature, as well as keep the similar characteristics of Y with its substitution of Sm. By lowering melting temperature of the alloy composition, we were aware that the contact angle of the liquid was also a critical parameter, as Halverson et al.[28] reported on Al infiltrating B<sub>4</sub>C. They determined that the contact angle of liquid Al decreased from 148° to 28° with increasing temperature from 1173 K (900°C) to 1573 K (1300°C), respectively. In addition, the time at temperature affected the contact angle though it was more dramatic at 1173 K (900°C) for which the contact angle decreased from 148° upon immediate contact with B<sub>4</sub>C to 22° after 1450 minutes. Upon considering the temperature differential above the melting temperature of the alloys and the reacting time, the Al-Sm-Me system was decided to study the reactive infusion into B<sub>4</sub>C.

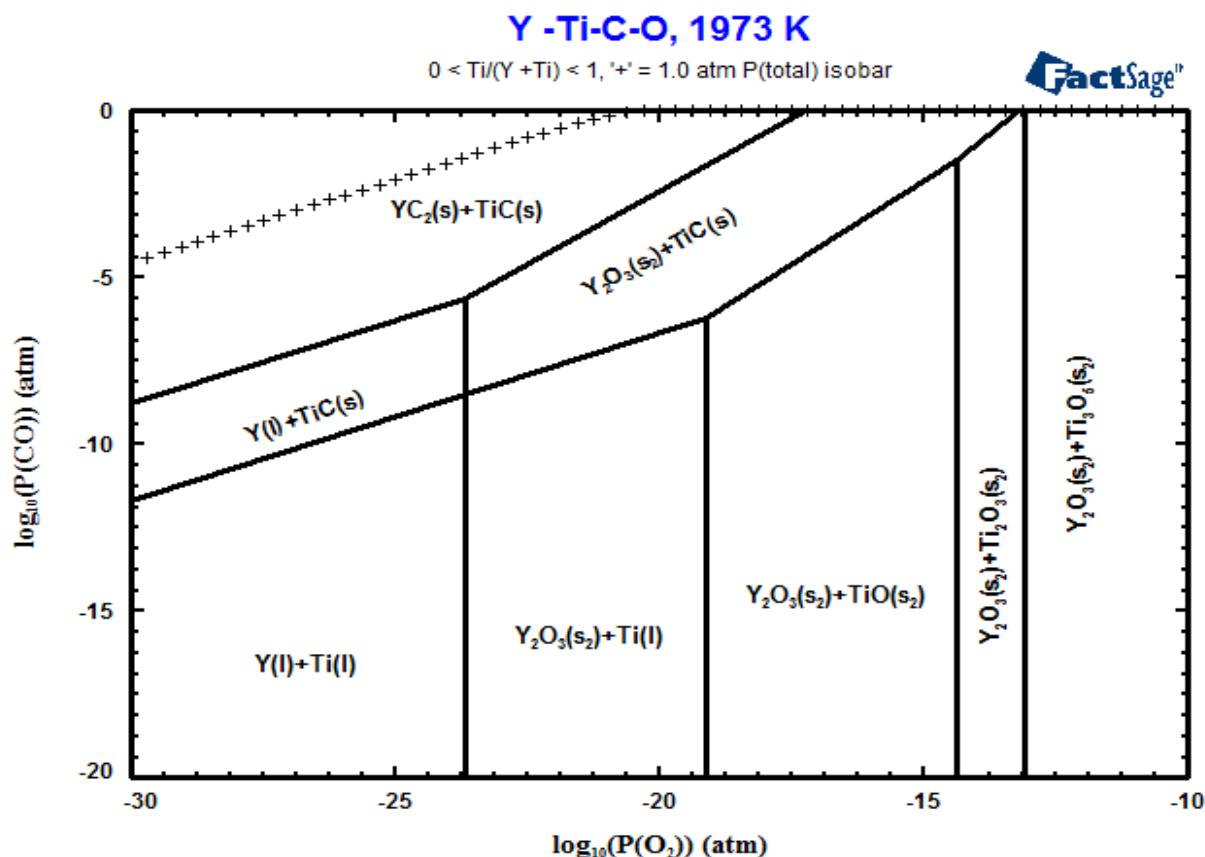


**Figure 18 -- Superimposed stability diagram of the Y-C-O and Ti-C-O systems at 1973K.**

In addition to oxygen potential, Ellingham diagrams best depict the stability of the carbides and borides compared to B<sub>4</sub>C, as shown in Figures 19 and 20. The carbides of Sm, Y and Ti are clearly more stable than B<sub>4</sub>C at temperatures greater than approximately 1473 K (1200°C). However, Al<sub>4</sub>C<sub>3</sub> may form upon cooling from 1973 K (1700°C) as the intersection of the B<sub>4</sub>C and Al<sub>4</sub>C<sub>3</sub> occurs near 773 K (500°C). As for the borides, AlB<sub>2</sub> is the only boride more

stable than  $B_4C$  except when the temperature is greater than approximately 1873 K (1600°C) at which  $B_4C$  is more stable than  $SmB_4$ . The borides and carbides for elements of the Hf family (Hf, Ti and Zr) are clearly more stable than  $B_4C$  as similarly to the oxides, which were reported by Maheswaraiah, Sandate and Bronson [9]. A comparison of the stability of carbides and borides of the elements used in the system is shown in the Figure 19 and 20

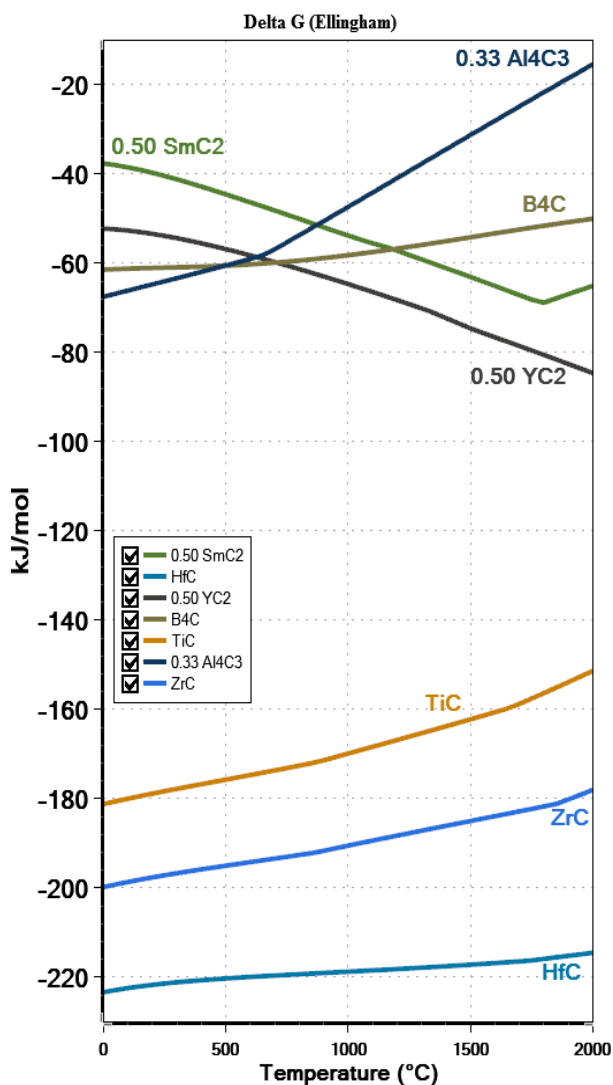


Figure 19 Stability of Carbides (HSC V8)

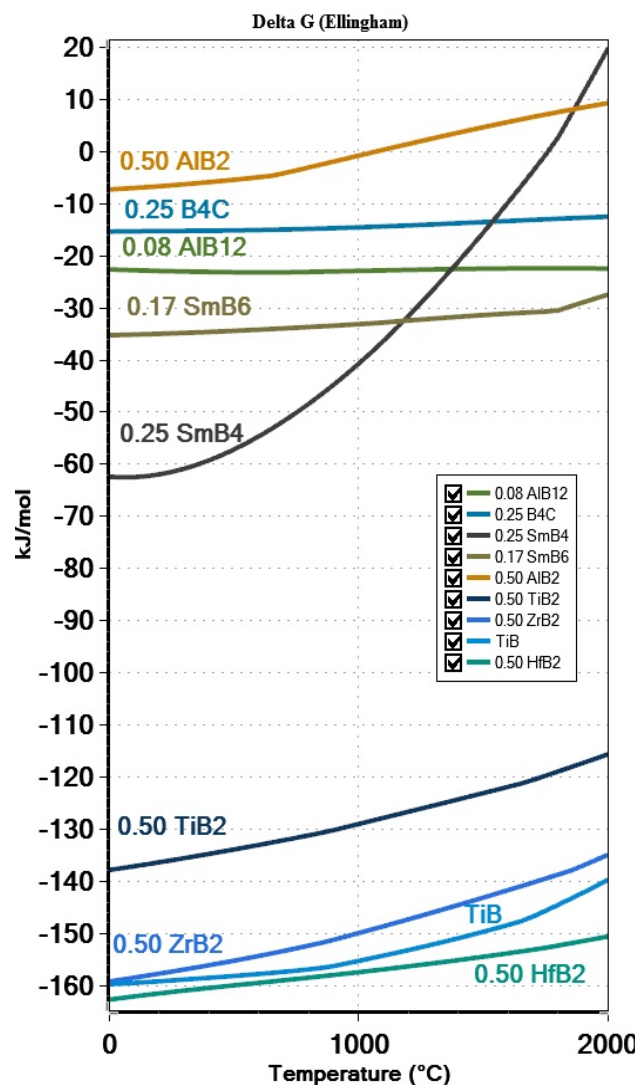
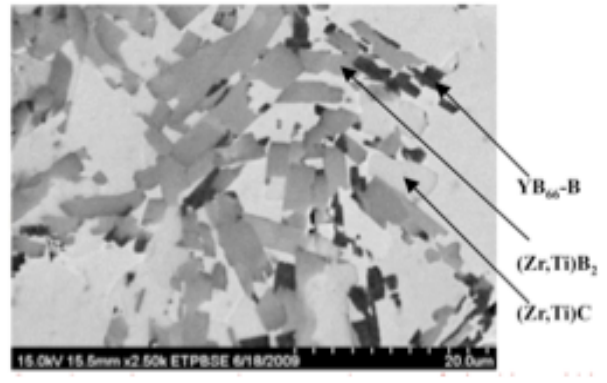
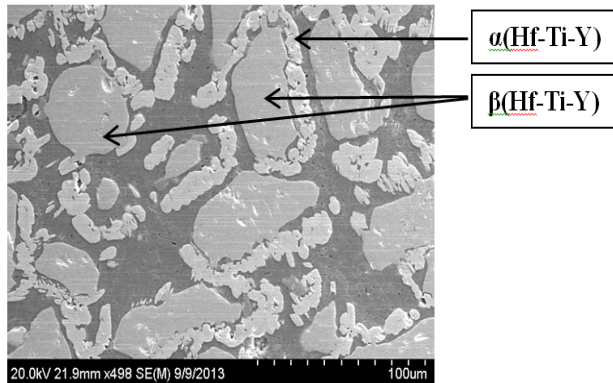


Figure 20 -- Stability of Borides (HSC V8)



## 2.8 Typical microstructures from experiments

Typical microstructures obtained after using the pseudo-isopiestic technique to control



**Figure 21 -- Microstructure of Ti-Y-Hf Alloy    Figure 22 -- Microstructure of Zr-Y-Ti/B<sub>4</sub>C**

oxygen potential for preparing the highly reactive elements (i.e., Ti-Y-Hf) and Zr-Y-Ti reacting with B<sub>4</sub>C are shown in Figure 21 and 22, respectively. The microstructure of Hf-Ti-Y alloy showed no formation of its oxides and the primary phases are the high temperature  $\beta$ -Hf phase, dissolved with Y and Ti in the expected body-centered cubic structure ( $\beta$ -phase), and the low temperature hexagonal closed packed ( $\alpha$ -phase). The remaining matrix consists of primarily the Ti-Y-Hf phase. For a Zr-Ti-Y melt reacting with B<sub>4</sub>C, the precipitates of boride and carbide within a Zr-Ti-Y matrix appear in Figure 22.

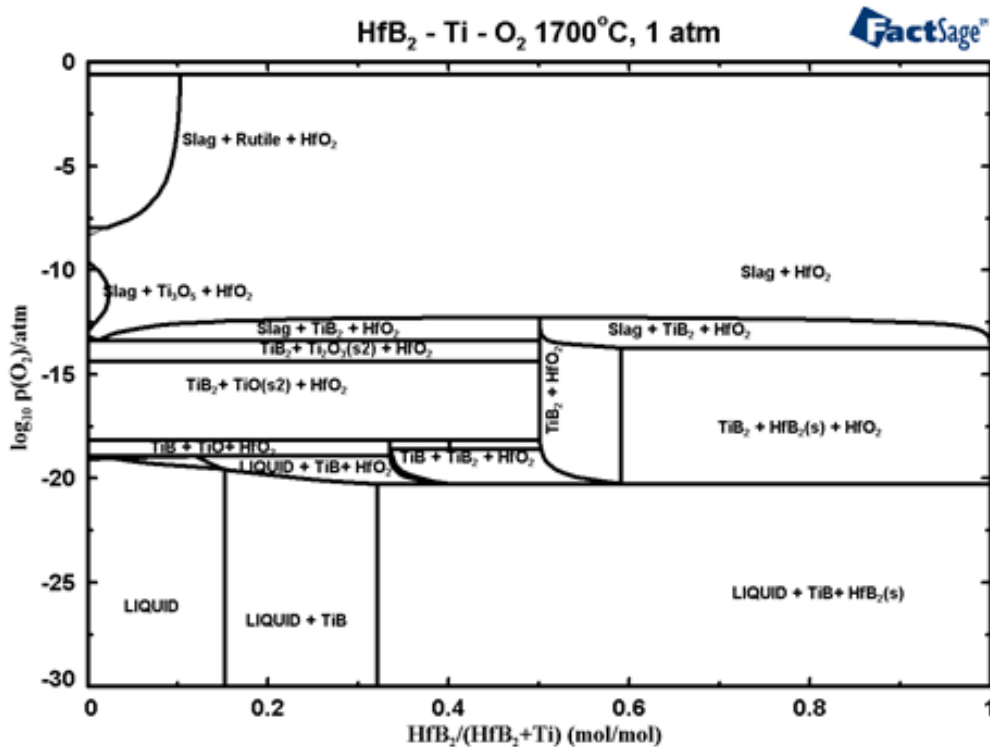


**Figure 23 -- Ti-HfB<sub>2</sub>-O<sub>2</sub> phase diagram indicating the oxygen potentials for the oxidation of TiB<sub>2</sub> and HfB<sub>2</sub> phases.**

Oxide precipitates were not found as an indication that the oxygen potential was sufficiently low without the formation of  $Y_2O_3$ . For the Hf component, the oxygen potential must be less than  $10^{-22}$  atm must be achieved to ensure no formation of  $HfO_2$  (Figure 23), as shown in the microstructure of Figure 24. Hafnium does precipitate along with  $Al_3Sm$  surrounded by the Al-Sm-Hf alloy though the expected  $Al_3Hf$  was curiously not distinguished in the microstructure.

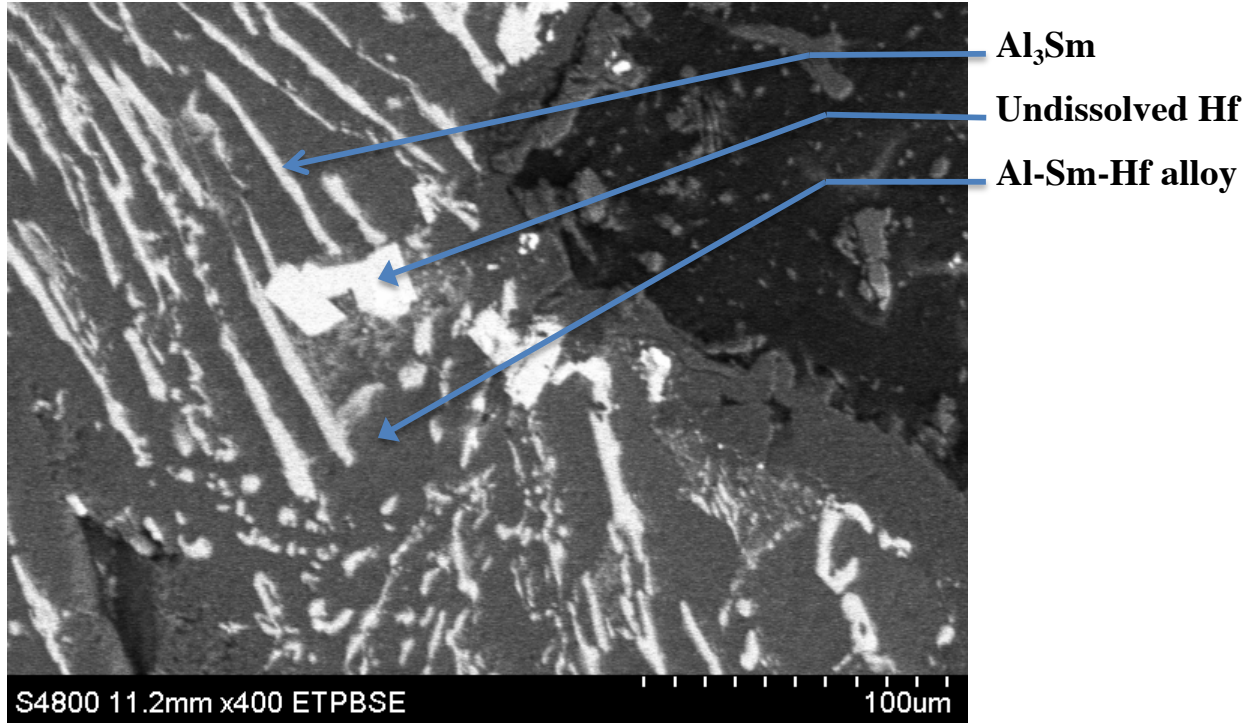


**Figure 24 -- 75Al-20Sm-5Hf alloy (content indicated in wt. %).**

The reaction of a liquid Al-Sm alloy with  $B_4C$  caused the formation of Al borides and carboborides, as shown in the microstructure of Figure 25 complemented with its line scan in Figure 26. The phases formed between Al-Sm and  $B_4C$  are identified in Figure 27. On the Al-B binary phase diagram, the formation of  $AlB_2$  occurs at 1229 K (956°C) via the following peritectic reaction:



With the formation of  $Al_3BC$ , the cooling the sample may have transformed the ternary structure of  $Al_3BC_3$ - $Al_{2.1}B_{5.1}C_8$ - $Al_L$  into  $Al_3BC$ .

The SEM image labeled as  $Al_3Sm$  phase (or  $\delta$ - $Al_3Sm$ ) with the hexagonal structure results from the following catatectic reaction:



The Al-Sm liquid forming from the solid  $\beta Al_4Sm$  phase with a tetragonal structure forms as it cools to precipitate the  $\delta$ - $Al_3Sm$ , as explained by Zhou and Napolitano [29] in their study of the

Al-Sm binary system. They also reported that the  $\alpha\text{Al}_{11}\text{Sm}_3$  phase is metastable when the  $\delta\text{Al}_3\text{Sm}$  precipitates.

The formation of carboborides and Sm borides were detected by the XRD spectrums with the alloys reacting with the  $\text{B}_4\text{C}$ . The possible reactions taking place in the system are shown in the following equations.



Halverson et al. the ternary Al-B-C at 1273 K. At lower temperatures, 1141 K, the formation of  $\text{Al}_3\text{BC}$  and  $\text{AlB}_2$  exists and at temperatures  $>1141\text{K}$   $\text{AlB}_2$ , because of its lower decomposition temperature of 1165K is replaced by  $\beta\text{-AlB}_{12}$ , which is also referred to as  $\text{Al}_3\text{B}_{48}\text{C}_2$  [30]. Though the Al- $\text{B}_4\text{C}$  study detailed particularly the Al-B-C ternary system, the microstructures clearly indicated the coexistence of the  $\text{AlB}_2$ ,  $\text{Al}_3\text{BC}$  and  $\text{B}_4\text{C}$ . However, in conferring with the Al-B system,  $\text{AlB}_2$  was precipitated after cooling from 1248K as Halverson has reported. Hence at temperatures greater than 1248K, the  $\text{AlB}_2$  phase exists. In addition,  $\text{B}_4\text{C}$  phases are either slightly surrounded by the  $\text{Al}_3\text{BC}$  phase suggesting seemingly peritectic type reaction or the reaction between liquid Al and  $\text{B}_4\text{C}$  to form  $\text{Al}_3\text{BC}$ .

The samarium-boron phase diagram exists with a few borides  $\text{SmB}_4$ ,  $\text{SmB}_6$  and  $\text{SmB}_{66}$  for which the peritectics of  $\text{SmB}_4$  and  $\text{SmB}_6$  are estimated.  $\text{SmB}_2$  which is not shown on the phase diagram was only reported to form at high pressures (6.5Gpa) [31].  $\text{SmB}_6$  has a congruent reaction with the liquid with a reported temperature of 2580°C. Similarly, the  $\text{SmB}_6$  with on reaction with the liquid is further leads to the formation of  $\alpha\text{SmB}_{66}$  with a peritectic temperature of 2150°C.

For the Al-Sm-Me reaction with  $\text{B}_4\text{C}$ , one must consider the Sm gas formation as shown in reaction 11. The XRD spectrums show the presence of the samarium hexaboride ( $\text{SmB}_6$ ), which may be the result of tetraboride to hexaboride conversion as described by Sturgeon and Eick [32]. The formation of  $\text{SmB}_6$  results in endothermic reaction ( $\Delta H = 1247 \text{ kJ @ } 1973\text{K}$ ) and the Gibbs free energy indicates a favorable reaction ( $\Delta G = -311 \text{ kJ}$ ). However, in the present study Sm vapor was not observed though possible.

Samarium forms a brittle dicarbide ( $\text{SmC}_2$ ) though very limited research is available for samarium and its use in alloys. Although a proper samarium-carbon binary system has been reported, but a review by Gschneider and Calderwood [33] lists more phases ( $\alpha\text{Sm}$ ,  $\beta\text{Sm}$ ,  $\gamma\text{Sm}$ ,  $\text{Sm}_3\text{C}$ ,  $\text{Sm}_2\text{C}_3$ ,  $\alpha\text{SmC}_2$ ,  $\beta\text{SmC}_2$ ) in a Sm-C system. The reaction of samarium with boron carbide results in the formation of  $\text{SmB}_4$  and C as shown in the reaction 9. The enthalpy of this reaction at 1973K is -430 kJ indicating the reaction is exothermic, but above 1808 K the reaction becomes unfavorable as the Gibbs free energy of the reaction is positive. The effect of Sm, which behaves similar to Y, on the reaction with  $\text{B}_4\text{C}$  to form Sm carbides and borides requires further study.



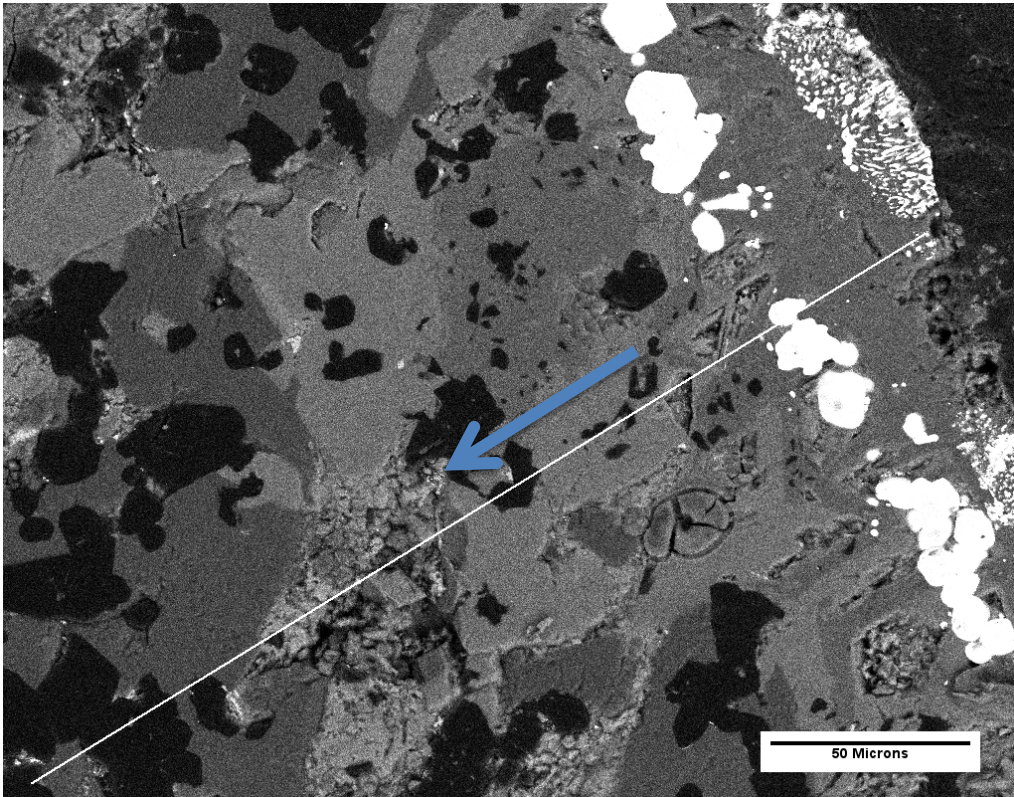


**Figure 25 -- Microstructure of a Al-Sm-Hf with B<sub>4</sub>C (80-15-5 wt. %) sample with a line scan**

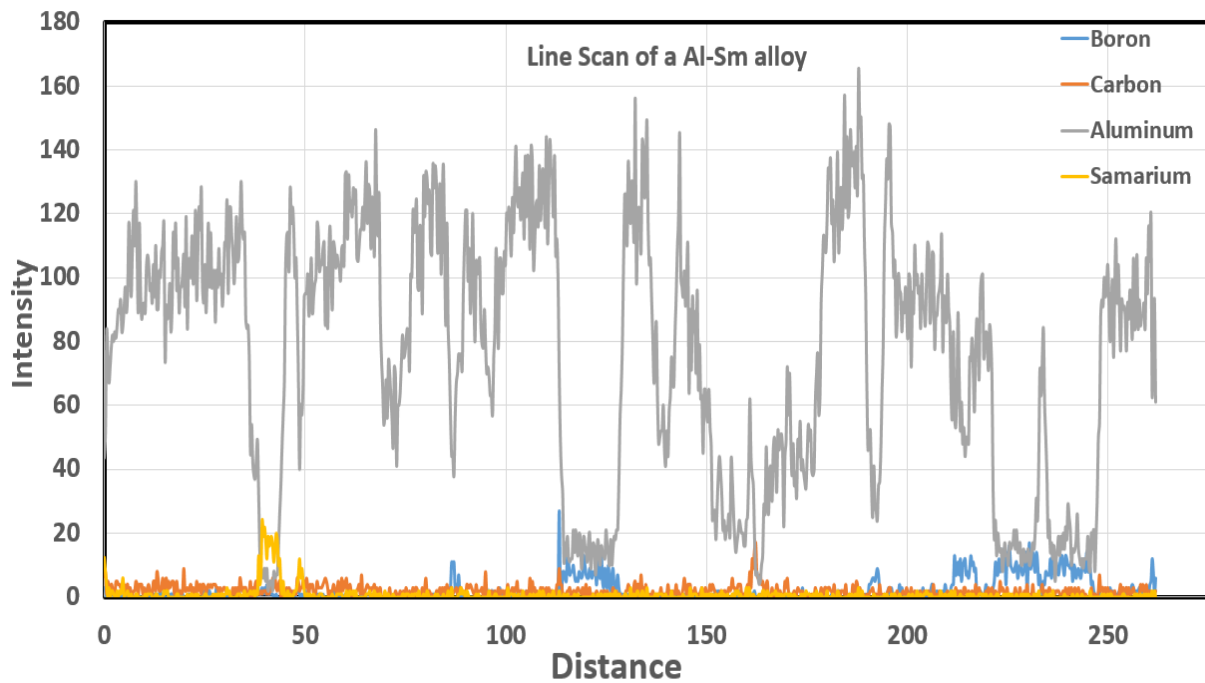


**Figure 26 -- Line scan analysis of the microstructure Al-Sm-Hf**

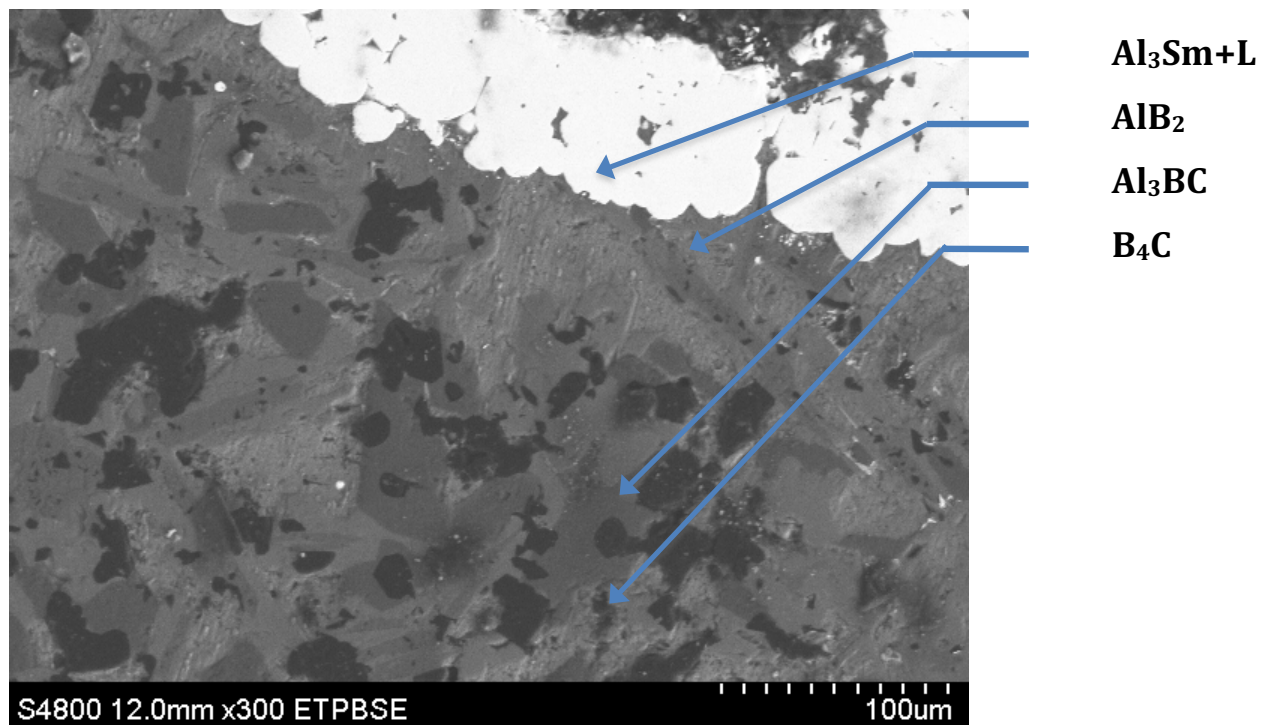


**Figure 27 -- Al-Sm alloy Al-Sm (74-26 wt. %) on  $B_4C$  acquired with a scanning electron microscope using backscattered electrons.**

**2.9. Objectives Achieved:** The objectives met during the research effort:

1. The infusion of liquid Hf, Ti and Y was simulated with a simple model of computational fluid dynamics by using Fluent software.
2. The pseudo-isopiestic technique was designed for investigation at  $1700^{\circ}C$  for the Hf-Ti-Y alloy melt reacting with  $B_4C$  though compositions limit the reactive infusion even though sometimes attaining or exceeding 2045 K ( $1772^{\circ}C$ ) because of the exothermic reaction.
3. Hf-Y-Ti master alloys have been prepared for use in melt infusion into  $B_4C$  packed bed. The key for alloys with yttrium is the minimization of the formation of  $Y_2C$  and  $YC_2$ .
4. Al-Sm liquid alloys infiltrated into a  $B_4C$  packed bed to form Al borides and Al carboborides at  $1700^{\circ}C$ .
5. A modified Semlak-Rhines equation was developed to simulate the effects of the capillary flow of the liquid as time decreases, and a maximum flow into the capillary is achieved at 0.1 to 1  $\mu s$  for liquid Hf, Sm, Ti, Y and Zr at their respective melting temperature.

**2.10. Future Goals:** The research tasks for the next phase of the research are as follows:

1. The Fluent software will include more pores for simulating the effect of adjacent pores connecting with each other.
2. Expand the extended finite volume code to incorporate the boride and carbide precipitates.
3. The experimental tasks at temperatures of 2000 to  $2500^{\circ}C$  could occur once an induction furnace is acquired to determine the effect of more reactive liquid alloys (i.e., Hf-Ti-Y-Re). Rare earth elements (e.g., Ce, Sm, Lu, Yb) may form carbide and borides to enhance the mechanical properties of HfC-HfB<sub>2</sub>-Hf composite.

### 3. Accomplishments/New Findings

**Accomplishments** -- The reactive processing of boride/carbide composites with a controlled oxygen potential was published in the International Journal of Applied Ceramic Technology. The methodology consists of a thermodynamic system equilibrating the Zr system at temperatures reaching near 2600°C with an Al system at approximately 700°C. The temperature gradient within a pseudo-isopiestic technique established the oxygen potential near 700°C. The processing technique is extended to form yttrium boride in a  $\text{HfB}_2\text{-HfC/Hf-Ti-Y}$  matrix, which would incorporate a boride complex in the composite with possible strength and oxidizing improvements. The methodology of controlling the oxygen potential successfully melted master 70Ti-Hf-Y alloys, but their infusion into  $\text{B}_4\text{C}$  packed bed has been problematic at 1700°C. With the analysis of the fluid dynamics for liquid Y, the temperature and pore size affects the penetrating rate as shown in Figure 13.

**Relevance to Air Force Mission** -- The computational fluid dynamics of the infusion of Hf alloy melts could optimize the placement of precipitates to improve mechanical and oxidizing properties for  $\text{HfB}_2\text{/HfC/Hf-Y-Ti}$  at 1700°C. The effects of surface energies, diffusion of components within the liquid phase, and interfacial reactions could be used to optimize the reactive infusion process. With the use of computational fluid dynamics in liquid processing of boride/carbide systems at 1700°C, the processing simulations of ceramic composites could predict the formation of stable and metastable phases to more extreme ultrahigh temperatures upon coupling of the modeling with thermodynamics.

### 4. Personnel Supported

Sanjay Shantha-Kumar and Arturo Medina were primarily supported with AFOSR funds for their doctoral and master's degrees, respectively. Sanjay Shantha-Kumar performed the strategic experimentation on the reactive infusion of Al-Sm, Al-Sm-Ti, Al-Sm-Hf, Al-Sm-Zr and Hf-Y-Ti melts into  $\text{B}_4\text{C}$ . He continues as a research associate at the University of Texas at El Paso after acquiring his doctoral degree. Arturo Medina computed the infusion by using Fluent software with his background in fluid mechanics and heat transfer. Arturo served as an intern to work on fluid mechanics and/or heat transfer at the Kirkland Air Force Base for the summers of 2014 and 2013. He joined the Federal Aviation Administration as a mechanical engineer for their technical staff after acquiring his master's degree.

### 5. Publications/Interactions

In 2012, Maheswaraiah, Sandate and Bronson [9] published on the reactive processing of the Zr alloy melts with  $\text{B}_4\text{C}$  with a controlled-oxygen potential. The continuation of the processing technique was presented at the Materials Science & Technology 2013 meeting in Montreal, Quebec, Canada at the session on Innovative Processing and Synthesis of Ceramics, Glasses and Composites. The title of our presentation was **“Rate of Reactive Infusion of Zr and Hf Alloy Melts into  $\text{B}_4\text{C}$  with Controlled Oxygen Potential and by Surface Tension Driven Flow.”** The computational analysis of the capillary infusion was recently submitted to Metallurgical and Materials Transactions with a manuscript entitled, **“High Temperature Liquid Metal Infusion Considering Surface Tension-Viscosity Dissipation.”**

The research group is collaborating with Dr. Erica Corral of the University of Arizona by preparing samples using a plasma-spark-sintering furnace. David Pham, a previous graduate

student who finished his master's degree with Professor Bronson, is pursuing his doctoral degree in Professor Corral's research group.

Professor Bronson visited Air Force Research Laboratory on March 27, 2014 to exchange technical views with Dr. Allan Katz and his colleagues on ultrahigh temperature ceramic composites. Dr. Bronson also presented a talk entitled, "**Reactivity of Zr and Hf Boride-Carbide-Oxide Systems at Ultrahigh Temperatures.**"

#### **6. Patent Disclosures/Awards**

No patent disclosures have been submitted, yet, though the university is reviewing a patent application for the processing of the reactive metals to control the oxygen potential.

#### **8. References**

1. J.-C. Zhao and J. H. Westbrook, MRS Bull. **28**, 622 (2003).
2. H. Petla, E. P. Renova, A. Bronson, J. F. Chessa, and N. Maheswaraiah, J. Eur. Ceram. Soc. **30**, 2407 (2010).
3. A. Bronson and J. Chessa, J. Am. Ceram. Soc. J. Am, Ceram, Soc. **91** [5], 1448 (2008).
4. F. Delanny, L. Froyen, and A. Deruyttere, J. Mater. Sci. **22**, 1 (1987).
5. N. Eustathopoulos, Acta Mater. **46**, 2319 (1998).
6. E. Saiz and A. P. Tomsia, Curr. Opin. Solid State Mater. Sci. **9**, 167 (2005).
7. R. E. Loehman, K. Ewsuk, and A. P. Tomsia, J. Am. Ceram. Soc. **79**, 27 (1996).
8. W. B. Johnson, A. S. Nagelberg, and E. Breval, J. Am. Ceram. Soc. **74**, 2093 (1991).
9. N. Maheswaraiah, A. V. Sandate, and A. Bronson, Int. J. Appl. Ceram. Technol. **10**, 234 (2013).
10. E. Saiz and A. P. Tomsia, Nat Mater **3**, 903 (2004).
11. E. Saiz, C.-W. Hwang, K. Suganuma, and A. P. Tomsia, Acta Mater. **51**, 3185 (2003).
12. N. Grigorenko and V. Poluyanskaya, "In Interfacial Sci. Ceram. Joining, Bellosi Al, Ed. **58**, 69 (1998).
13. C. H. P. Lupis, *Chemical Thermodynamics of Materials* (Elsevier Science Publishers, New York, 1983).
14. M. Benhassine, E. Saiz, A. P. Tomsia, and J. De Coninck, Acta Mater. **59**, 1087 (2011).
15. T. P. Swiler and R. E. Loehman, Acta Mater. **48**, 4419 (2000).
16. P. Delgado and V. Kumar, Appl. Math. Comput. **266**, 328 (2015).

17. P. Delgado and V. Kumar, in *ASME 2013 Fluids Eng. Div. Summer Meet.* (American Society of Mechanical Engineers, 2013), p. V01CT23A001.
18. F. N. Semlak, K.A. Rhines, *Trans. Met. Soc. AIME* **21**, 325 (1958).
19. G. P. Martins, D. L. Olson, and G. R. Edwards, *Metall. Trans. B* **19**, 95 (1988).
20. J. R. Ligenza and R. B. Bernstein, *J. Am. Chem. Soc.* **73**, 4636 (1951).
21. P. Paradis, T. Ishikawa, G. Lee, D. Holland-Moritz, J. Brillo, W. Rhim, and J. T. Okada, *Mater. Sci. Eng. R Reports* **76**, 1 (2014).
22. T. Ishikawa, P. Paradis, J. T. Okada, and Y. Watanabe, *Meas. Sci. Technol.* **23**, 025305 (2012).
23. T. B. Massalski, H. Okamoto, P. R. Subramanian, and L. Kacpack, *Binary Alloy Phase Diagrams*, 2nd. Editi (ASM Internaitonal, Metals Park, 1990).
24. P. F. Paradis, T. Ishikawa, and N. Koike, *Microgravity Sci. Technol.* **21**, 113 (2008).
25. B. Gallois and C. H. P. Lupis, *Metall. Trans. B* **12**, 549 (1981).
26. C. Wagner, in *Nachrichten Der Akad. Der Wissenschaften Zu Göttingen*, Mathematis (Vandenhoeck and Ruprecht, Gottingen, 1973), pp. 1–27.
27. R. . Hondros, E. D, Edited by Rapp, in *Tech. Met. Res.* (1970), pp. 293–348.
28. D. Halverson, A. J. Pyzik, Ilhan A. Aksay, and W. E. Snowden, *J. Am. Ceram Soc.*, **72[5]**, 775 (1989).
29. S. H. Zhou and R. E. Napolitano, *Metall. Mater. Trans. A* **38**, 1145 (2007).
30. J. Viala, J. Bouix, G. Gonzalez, and C. Esnouf, *J. Mater. Sci.* **2**, 4559 (1997).
31. P. K. Liao and K. E. Spear, *J. Phase Equilibria* **16**, 521 (1995).
32. G. D. Sturgeon and H. A. Eick, *J. Physical Chemistry*, **69**, 3705-3708 (1966).
33. C. References, B. K. A. Gschneidner, and F. W. Calderwood, **7**, 560 (1986).

## 8. Appendices

In this appendix, steps involved in solving the modified SR equation are presented. We start with the Eq.(3) with the appropriate initial conditions.

$$\frac{d}{dt} \left( (\rho\pi R^2 h + \rho V_L) \frac{dh}{dt} \right) = 2\pi R \sigma \cos(\theta) - 8\pi\mu(h + h_0) \left( \frac{dh}{dt} \right) \quad (3)$$

$$-\rho(\pi R^2 h + V_L)g - \frac{1}{4}\rho\pi R^2 \left(\frac{dh}{dt}\right)^2$$

$$h|_{t=0} = 0; \left.\frac{dh}{dt}\right|_{t=0} = 0 \quad (4)$$

Dividing Eq. (3) by  $\pi R^2$  yields

$$\rho \frac{d}{dt} \left( \{h + R\tilde{V}_L\} \frac{dh}{dt} \right) = 2\pi\sigma \cos(\theta) / R - 8\mu(h + h_0)R^{-2} \frac{dh}{dt} - \rho g(h + R\tilde{h}_L) - \frac{1}{4}\rho \left(\frac{dh}{dt}\right)^2 \quad (5)$$

$$\text{with } \tilde{V}_L = V_L / (\pi R^3); \tilde{h}_L = h_L / R$$

Eq. (5) may be written in the form

$$\rho \frac{d}{dt} \left( \{h + R\tilde{V}_L\} \frac{dh}{dt} \right) = \rho g(h_e - h) - 8\mu(h + h_0)R^{-2} \frac{dh}{dt} - \frac{1}{4}\rho \left(\frac{dh}{dt}\right)^2 \quad (6)$$

where  $h_e$  is the equilibrium capillary height given by

$$h_e = \frac{2\sigma \cos(\theta)}{\rho g R} - R\tilde{h}_L \quad (7)$$

Dividing by the density  $\rho$ , we get

$$\frac{d}{dt} \left( \{h + R\tilde{V}_L\} \frac{dh}{dt} \right) = g(h_e - h) - \frac{8\mu(h + h_0)}{\rho R^2} \frac{dh}{dt} - \frac{1}{4} \left(\frac{dh}{dt}\right)^2 \quad (8)$$

As small time, the rate of penetration is small and hence contributions from the  $h_0$  can be ingored.

We introduce the following non-dimensional capillary height and time

$$\tilde{h} = h / h_e; \tau = t \sqrt{g / h_e} \quad (9)$$

$$\text{Then } gh_e \frac{d}{d\tau} \left( \{\tilde{h} + (R / h_e)\tilde{V}_L\} \frac{d\tilde{h}}{d\tau} \right) = gh_e(1 - \tilde{h}) - \frac{8\mu\sqrt{gh_e}}{\rho R^2} \tilde{h} \frac{d\tilde{h}}{d\tau} - \frac{1}{4} gh_e \left(\frac{d\tilde{h}}{d\tau}\right)^2 \quad (10)$$

Dividing by  $gh_e$ , we obtain

$$\frac{d}{d\tau} \left( \{\tilde{h} + (R / h_e)\tilde{V}_L\} \frac{d\tilde{h}}{d\tau} \right) = (1 - \tilde{h}) - 8\tilde{\mu}\tilde{h} \frac{d\tilde{h}}{d\tau} - \frac{1}{4} \left(\frac{d\tilde{h}}{d\tau}\right)^2 \quad (11)$$

$$\text{where } \tilde{\mu} = \mu / (\rho R^2 \sqrt{gh_e}) \quad (12)$$

Writing  $\tilde{v}$  for  $d\tilde{h} / d\tau$  and using the fact that

$$\frac{d^2\tilde{h}}{d\tau^2} = \frac{d}{d\tilde{h}} \left( \frac{1}{2} \tilde{v}^2 \right) \quad (13)$$

we have

$$(\tilde{h} + \alpha) \frac{d}{d\tilde{h}} \left( \frac{1}{2} \tilde{v}^2 \right) + \frac{5}{4} \tilde{v}^2 = (1 - \tilde{h}) - 8\tilde{\mu}\tilde{h}\tilde{v} \quad (14)$$

$$\text{with } \alpha = R\tilde{V}_L / h_e \quad (15)$$

Eq. (14) can be written as

$$\frac{d}{d\tilde{h}} \left\{ (\tilde{h} + \alpha)^{5/2} f \right\} = \left\{ (1 - \tilde{h}) - 8\tilde{\mu}\tilde{h}\sqrt{2f} \right\} (\tilde{h} + \alpha)^{3/2} \quad (15)$$

$$\text{with } f(\tilde{h}) = \frac{1}{2} \tilde{v}^2 \quad (16)$$

Eq. (12) is subject to the initial condition

$$f(0) = 0 \quad (17)$$

*Special Case -  $\tilde{\mu} = 0$*

In this case Eq. (15) may be integrated explicitly, using Eq. (17), to obtain

$$(\tilde{h} + \alpha)^{5/2} f = \frac{2}{5} (1 + \alpha) \left\{ (\tilde{h} + \alpha)^{5/2} - \alpha^{5/2} \right\} - \frac{2}{7} \left\{ (\tilde{h} + \alpha)^{7/2} - \alpha^{7/2} \right\} \quad (18)$$

This yields

$$f = \frac{2}{5} (1 + \alpha) - \frac{2}{7} (\tilde{h} + \alpha) - \beta / (\tilde{h} + \alpha)^{5/2} \quad (19)$$

$$\text{with } \beta = \frac{2}{5} \alpha^{5/2} (1 + \frac{2}{7} \alpha) \quad (20)$$

Note that, as  $\tilde{h}$  rises from zero,  $f$  increases from zero to a maximum and then falls back to zero again, at the maximum value of  $\tilde{h}$ . Since  $\alpha$  is very small in comparison with unity, we have, approximately,

$$\tilde{h}_{\max} = \frac{7}{5} + \frac{2}{5} \alpha \quad (21)$$

A better approximation is

$$\begin{aligned} \tilde{h}_{\max} &= \frac{7}{5} + \frac{2}{5} \alpha - \frac{7}{5} \alpha^{5/2} \frac{1 + \frac{2}{7} \alpha}{\left\{ \frac{7}{5} (1 + \alpha) \right\}^{5/2}} \\ &= \frac{7}{5} + \frac{2}{5} \alpha - \frac{5}{7} \sqrt{\frac{5}{7}} \alpha^{5/2} \frac{1 + \frac{2}{7} \alpha}{(1 + \alpha)^{5/2}} \end{aligned} \quad (22)$$

Noting that  $\tilde{h}_{\max}$  is larger than the equilibrium value of  $\tilde{h}_{\max} = 1$ , we see that the system is underdamped. We now compute the maximum value of  $f$  and hence the fluid velocity. Let  $\tilde{h} = \tilde{h}_0$  when  $f$  is maximized. The value of  $\tilde{h}_0$  is obtained by setting the derivative of  $f$  to zero.

$$\frac{df}{d\tilde{h}} \bigg|_{\tilde{h}=\tilde{h}_0} = -\frac{2}{7} + \frac{5}{2} \beta / (\tilde{h}_0 + \alpha)^{7/2} = 0 \quad (23)$$

$$\text{Hence } \beta / (\tilde{h}_0 + \alpha)^{5/2} = \frac{4}{35} (\tilde{h}_0 + \alpha) \quad (24)$$

Substituting Eq. (24) back into Eq. (19), with  $\tilde{h}$  set to  $\tilde{h}_0$  we get

$$f_{\max} = \frac{2}{5} (1 - \tilde{h}_0) \quad (25)$$

Now, from Eq. (19),

$$(h_0 + \alpha)^{7/2} = \frac{7}{2} \alpha^{5/2} (1 + \frac{2}{7} \alpha)$$

$$\text{Then } \tilde{h}_0 = \left( (1 + \frac{2}{7} \alpha) \frac{7}{2} \alpha^{5/2} \right)^{2/7} - \alpha \quad (26)$$

*General  $\mu$*

In this case Eq. (15) needs to be solved numerically, subject to the initial condition in Eq. (10). To do this, we divide the range of  $\tilde{h}$  into intervals  $[\tilde{h}_{k-1}, \tilde{h}_k]$ ;  $k = 1, 2, \dots, N$ , with  $\tilde{h}_k = 0$ ,  $\tilde{h}_N = \tilde{h}$ . Let

$$f_k = f(\tilde{h}_k) \quad (27)$$

For  $\tilde{h}_k \leq \tilde{h} < \tilde{h}_{k+1}$  (28)

Eq. (15) is approximated by

$$\frac{d}{d\tilde{h}} \left\{ (\tilde{h} + \alpha)^{5/2} f \right\} = (1 - \tilde{h})(\tilde{h} + \alpha)^{3/2} - 8\tilde{\mu}\tilde{h}(\tilde{h} + \alpha)^{3/2} \sqrt{2f_k}; \tilde{h}_k \leq \tilde{h} < \tilde{h}_{k+1} \quad (29)$$

Eq. (29) is solved subject to the initial condition

$$f(h_k) = f_k \quad (30)$$

Note that Eq. (29) may be written in abbreviated form as

$$\frac{d}{d\tilde{h}} \left\{ (\tilde{h} + \alpha)^{5/2} f \right\} = (1 - B_k \tilde{h})(\tilde{h} + \alpha)^{3/2}; \tilde{h}_k \leq \tilde{h} < \tilde{h}_{k+1} \quad (31)$$

with  $B_k = 1 + 8\tilde{\mu}\sqrt{2f_k}$  (32)

Integrating Eq. (31) over the interval  $[h_k, h_{k+1}]$  yields the result

$$\begin{aligned} (\tilde{h}_{k+1} + \alpha)^{5/2} f_{k+1} - (\tilde{h}_k + \alpha)^{5/2} f_k &= \frac{2}{5} (1 + B_k \alpha) (\tilde{h}_{k+1} + \alpha)^{5/2} - \frac{2}{7} B_k (\tilde{h}_{k+1} + \alpha)^{7/2} \\ &\quad - \frac{2}{5} (1 + B_k \alpha) (\tilde{h}_k + \alpha)^{5/2} - \frac{2}{7} B_k (\tilde{h}_k + \alpha)^{7/2} \end{aligned} \quad (33)$$